Upscale Impact of Mesoscale Convective Systems and its Parameterization in an Idealized GCM for a MJO Analog above the Equator

Qiu Yang*

Center for Prototype Climate Modeling, New York University Abu Dhabi, Saadiyat Island, Abu Dhabi, UAE

Andrew J. Majda

Department of Mathematics and Center for Atmosphere Ocean Science, Courant Institute of Mathematical Sciences, New York University, New York, NY, USA,

Center for Prototype Climate Modeling, New York University Abu Dhabi, Saadiyat Island, Abu Dhabi, UAE

Mitchell W. Moncrieff

National Center for Atmospheric Research, Boulder, Colorado, USA

**Corresponding author address:* Qiu Yang, Courant Institute of Mathematical Sciences, New York University, 251 Mercer Street, New York, NY, 10012

E-mail: yangq@cims.nyu.edu

ABSTRACT

The Madden-Julian oscillation (MJO) typically contains several superclusters and numerous embedded mesoscale convective systems (MCSs). It is hypothesized here that the poorly simulated MJOs in current coarse resolution global climate models (GCMs) is related to the inadequate treatment of unresolved MCSs. So its parameterization should provide the missing collective effects of MCSs. However, a satisfactory understanding of the upscale impact of MCSs on the MJO is still lacking. A simple two-dimensional multicloud model is used as an idealized GCM with clear deficiencies. Eddy transfer of momentum and temperature by the MCSs, predicted by the mesoscale equatorial synoptic dynamics (MESD) model, is added to this idealized GCM. The upscale impact of westward-moving MCSs promotes eastward propagation of the MJO analog, consistent with the theoretical prediction of the MESD model. Furthermore, the upscale impact of upshear-moving MCSs significantly intensifies the westerly wind burst, due to two-way feedback between easterly vertical shear and eddy momentum transfer with low-level eastward momentum forcing. Finally, a basic parameterization of upscale impact of upshear-moving MCSs modulated by deep heating excess and vertical shear strength is provided as a new parameterization. This significantly improves key features of the MJO analog in the idealized GCM with clear deficiencies. A three-way interaction mechanism between the MJO analog, parameterized upscale impact of MCSs and background vertical shear is identified.

1. Introduction

The MJO is the dominant component of tropical intraseasonal variability (Zhang 2005) and dramatically impacts local weather through extreme rainfall and mid-latitude atmospheric conditions by tropical-extratropical teleconnection (Zhang 2013; Stan et al. 2017; Henderson et al. 2017). Tropical convection associated with the MJO is hierarchically organized across multiple spatial and temporal scales. The MJO typically contains multiple eastward- and westward-moving superclusters of cloudiness (Nakazawa 1988; Chen et al. 1996) with numerous embedded MCSs (Houze 2004) and cumulus clouds on smaller scales. As the major rainfall producer in the tropics, MCSs contribute up to 50% of the rainfall in most tropical regions (Tao and Moncrieff 2009). Although the effects of large-scale atmospheric conditions on the modulation of MCSs have been well documented in observations (Lin and Johnson 1996; Chen et al. 1996; LeMone et al. 1998), a satisfactory understanding of the collective effects of MCSs on the momentum and heat budgets of the MJO is still lacking.

It is hypothesized that the poorly simulated MJOs in current coarse resolution GCMs are related to the inadequate treatment of MCSs and their upscale impact. The essential difference between MCSs and smaller individual convective towers lies in the fact that the former typically have front-to-rear tilted organized structures, while the latter are unorganized (Moncrieff and Klinker 1997). Typical behavior of the poorly simulated MJOs in the GCMs includes impersistent eastward propagation, unrealistic planetary/intraseasonal variability in precipitation and winds, and upright vertical structure with a negligible westerly wind burst (WWB) (Jiang et al. 2015). In contrast, global cloud-resolving simulations that resolve MCSs successfully capture some key features of the MJOs (Grabowski 2003; Miura et al. 2007), and motivated the development of the superparameterization method based on two-dimensional cloud resolving models (CRMs) (Grabowski 2001, 2004; Randall et al. 2003; Majda 2007a) and a sparse space-time technique (Xing et al. 2009). Nevertheless, the computational cost to explicitly resolve MCSs is too expensive to be practical in long GCM simulations. An alternative way to address this issue is to develop new parameterizations for coarse-resolution GCMs that capture the upscale impact of unresolved MCSs on the MJO.

Several studies have assessed the upscale impact of MCSs based on observational measurement, reanalysis dataset and cloud-resolving simulations, most of which focus on convective momentum transfer (CMT) (Moncrieff 1981; LeMone 1983; Moncrieff 1992; LeMone and Moncrieff 1994). Convective-scale CMT by unorganized convection normally has frictional effects that reduce large-scale vertical shear (Zhang and McFarlane 1995). In contrast, mesoscale CMT by organized convection over hundred kilometers in horizontal scale can have countergradient momentum transport that enhances the large-scale vertical shear (Moncrieff 1981, 1992). Tung and Yanai (2002a) concluded that CMT is, on the average, downgradient over the western Pacific warm pool but upgradient during the westerly wind phase of the MJO (Tung and Yanai 2002b). Oh et al. (2015) found that the subgrid-scale and mesoscale CMT associated with the MJO has a distinctive three-layer vertical structure. Grabowski and Moncrieff (2001) demonstrated that CMT from westward-moving MCSs embedded in the eastward-moving convective envelope promotes the large-scale organization of convection. Inspired by multi-scale organization and the observed statistical self-similarity of tropical convection, Majda (2007b) systematically derived multi-scale asymptotic models that describe scale-interactions among clusters, superclusters and intraseasonal oscillations and highlight the crucial role of eddy transfer of momentum and temperature. Brenowitz et al. (2018) concluded that mesoscale CMT dominates the total vertical flux feedback on planetary-scale kinetic energy budget, providing new mechanisms for the planetary-scale organization of convection.

From a theoretical perspective, several modeling studies have sought to better understand the upscale impact of MCSs on the large-scale organization of tropical convection. Majda and Stechmann (2009) utilized a simple dynamic model with features of CMT from convectively coupled gravity waves and their interactions with large-scale mean flow. Khouider et al. (2012) demonstrated that in the active region of the MJO with WWB, CMT from both convectively coupled Kelvin waves (CCKWs) and MCSs plays a significant role in accelerating the low-level westerly winds. The three-dimensional mesoscale equatorial synoptic dynamic (MESD) model, originally derived by Majda (2007b), was used as a multi-scale framework to assess the upscale impact of MCSs on eastward-moving CCKWs (Yang and Majda 2018b) and westward-moving 2-day waves (Yang and Majda 2018a). Explicit expressions for eddy transfer of momentum and temperature obtained from the MESD model are an essential basis for the parameterization of upscale impact of MCSs provided here. Moncrieff et al. (2017) introduced the multi-scale coherent structure parameterization (MCSP) that achieved significant improvement in tropical precipitation patterns and precipitation variability in a GCM. In general, idealized models that simulate some key features of the MJO can serve as a useful testbed. Here we refer to these MJO-like events arising from the idealized models as the MJO analog.

The goals of this paper include the following three aspects: first, use a simple multicloud model for the MJO analog and intraseasonal variability above the equator to mimic the typical behavior of GCMs with clear deficiencies. Secondly, assess the upscale impact of MCSs on key features of the MJO analog, including persistent propagation of a two-scale structure, realistic planetary/intraseasonal variability in precipitation and winds, and a significant WWB. Thirdly, introduce a basic parameterization of upscale impact of MCSs and test its effects in the idealized GCM to address deficiencies.

In general, the multicloud models represent three dominant cloud types (congestus, deep, stratiform) by using the first- and second-baroclinic vertical modes and build the life-cycle of these cloud types into the convective heating closure through a switch function for mid-latitude dryness (Khouider and Majda 2006c, 2007, 2006a). The deterministic version of the multicloud models successfully captures characteristic features of CCEWs (Khouider and Majda 2008b, 2006b, 2008a) and the diurnal cycle (Frenkel et al. 2011a,b, 2013). The stochastic version captures the MJO (Khouider et al. 2010; Deng et al. 2015; Goswami et al. 2017) when coupled to the GCM. In this paper, we use a deterministic two-dimensional multicloud model for the MJO analog and intraseasonal variability above the equator (Majda et al. 2007; Harlim and Majda 2013). By reducing the magnitude of both congestus and stratiform heating, this model mimics the typical behavior of GCMs with clear deficiencies, where both convection types are underestimated (Seo and Wang 2010; Del Genio et al. 2012; Lappen and Schumacher 2012; Del Genio et al. 2015). In order to introduce the upscale impact of MCSs, we use explicit expressions for the eddy transfer of momentum and temperature theoretically predicted by the MESD model (Yang and Majda 2018b).

The upscale impact of MCSs on the MJO analog is assessed through comparison experiments with/without adding extra eddy transfer of momentum and temperature. The modulation effects of deep heating excess on eddy transfer of momentum and temperature are considered in order to mimic the scenario that MCSs are prominent in the active convection region of the MJO (Khouider et al. 2012). The results show that the upscale impact of westward-moving MCSs promotes the eastward propagation of the MJO analog, consistent with the theoretical prediction by the MESD model (Yang and Majda 2018b). The modulation effects of vertical shear are considered to mimic the observation that MCSs typically move towards the convection center (Lin and Johnson 1996; Chen et al. 1996; Moncrieff and Klinker 1997; Yanai et al. 2000; Houze Jr et al. 2000). The results show that the upscale impact of upshear-moving MCSs leads to a significant WWB in the middle and west of the MJO analog, due to the positive feedback between large-scale easterly vertical shear and embedded eddy momentum transfer with low-level eastward momentum forcing. Finally, we provide a basic parameterization of upscale impact of upshear-moving MCSs, where modulation effects of deep heating effects and vertical shear strength are linearly combined. Significant improvement is achieved by adding this parameterization to the idealized GCM that has clear deficiencies. A further simulation illustrates a three-way interaction mechanism between the MJO analog, parameterization of upscale impact of MCSs and background mean flow over a long time scale. Specifically, the resulting oscillatory background mean flow resembles the QBO-like oscillation identified in cloud resolving simulations (Held et al. 1993; Nishimoto et al. 2016) and simplified GCMs (Horinouchi and Yoden 1998).

The results of this paper are presented as follows. Section 2 summarizes the governing equations and properties of the two-dimensional multicloud model, including the realistic MJO analog above the equator and the idealized GCM that has clear deficiencies. Section 3 discusses the effects of eddy transfer of momentum and temperature from MCSs on the MJO analog. Section 4 provides a basic parameterization of upscale impact of upshear-moving MCSs under the modulating effects of deep heating excess and vertical shear strength, and tests its effects in the idealized GCM that has clear deficiencies. The paper concludes with discussion in Section 5.

2. An Idealized GCM for a MJO Analog and Intraseasonal Variability above the Equator

In this section, we briefly review the equations governing the multicloud model and the convective heating closure. The simple two-dimensional multicloud model used here (Majda et al. 2007; Harlim and Majda 2013) captures the MJO analog and intraseasonal variability above the equator. The goals of this section are to reproduce: i) a realistic MJO analog above the equator as a proxy for the observations, and ii) a simulation with reduced congestus and stratiform heating as an idealized GCM having clear deficiencies.

a. Governing equations and multicloud model parameterization

The multicloud models describe the life-cycle of three main cloud types (congestus, deep and stratiform) (Johnson et al. 1999) and incorporate it in the convective heating closure by using a switch function for mid-tropospheric dryness. Specifically, shallow congestus convection is first initialized with low-level heating (upper-level cooling), moistening the lower troposphere and preconditioning the deep convection. Then deep convection warms the whole troposphere due to extreme rainfall, followed by stratiform convection with upper-level latent heating and low-level cooling by rain evaporation (Khouider and Majda 2008b).

The governing equations and multicloud convective parameterization in dimensionless units are listed in Table 1 and Table 2, and all relevant parameters in Table 3. All physical variables are nondimensionalized by the following synoptic scaling: first-baroclinic dry Kelvin wave speed $c = N\frac{H_T}{\pi} = 50ms^{-1}$ for horizontal velocity, equatorial Rossby deformation radius $L = \sqrt{\beta c} = 1500km$ for length, $T = \frac{L}{c} = 8hrs$ for time, $\bar{\alpha} = \frac{H_T\Theta_0}{\pi g}N^2 = 15K$ for temperature, and $\frac{\alpha}{T} = 45Kday^{-1}$ for heating. For convenience, the moisture anomaly has the unit of temperature in K. Correspondingly, as the moisture sink, the precipitation has the unit of heating in $Kday^{-1}$.

Consistent with the first-baroclinic deep heating and the second-baroclinic consgestus/stratiform heating, both momentum and temperature variables in the free troposphere are truncated to the first- and second-baroclinic modes using the following Galerkin projection,

$$f = f_1\left[\sqrt{2}\cos(z)\right] + f_2\left[\sqrt{2}\cos(2z)\right], \quad f \in \{u, p, F^u\} \tag{1}$$

$$g = g_1\left[\sqrt{2}\sin(z)\right] + g_2\left[2\sqrt{2}\sin(2z)\right], \quad g \in \{\theta, S^\theta, F^\theta\} \tag{2}$$

where the vertical coordinate z is scaled by 5 km so that $z = 0, \pi$ in dimensionless units correspond to the surface (0 km) and top of the troposphere ($5\pi \approx 15.7$ km), respectively. Here u is zonal velocity, p is the pressure perturbation, F^u is eddy momentum transfer, θ is potential temperature anomaly, S^θ is heating, and F^θ is eddy heat transfer. As shown by Table 1, the first- and second-baroclinic momentum is forced by linear momentum damping mimicking boundary-layer turbulent drag $-\frac{C_d u_0}{h_b} u_j$, Rayleigh friction $-\frac{1}{\tau_R} u_j$, and eddy momentum transfer F^u_j. The first-baroclinic potential temperature is driven by the deep heating P, and the second-baroclinic potential temperature by congestus and stratiform heating $-H_s + H_c$. Both are further forced by radiative cooling $-Q^0_{R,j} - \frac{1}{\tau_D}\theta_j$ and eddy heat transfer F^θ. These dynamical fields are coupled to a column-integrated moisture perturbation (Khouider and Majda 2006b), where both linear and nonlinear moisture advection terms are retained and precipitation $-\frac{2\sqrt{2}}{\pi}P$ and downdrafts $\frac{D}{H_T}$ are added as moisture sink and source, respectively. Specifically, the precipitation in dimensionless units, $-\frac{2\sqrt{2}}{\pi}P$, is assumed to be equal to the total column-integrated heating, contributed by the first-baroclinic mode. The boundary-layer equivalent potential temperature equation shows that surface-level evaporation $\frac{E}{h_b}$ warms and moistens the boundary layer while the downdrafts $\frac{D}{h_b}$ have the opposite effects. Both congestus heating H_c and stratiform heating H_s are governed by linear relaxation equations. Congestus heating is triggered in the leading cold and dry mid-troposphere, and stratiform heating lags the deep heating region. A switch function for mid-troposphere dryness Λ is defined in Table 2. The multicloud heating closure is completed by introducing deep heating P, downdrafts D and evaporation E.

All physical variables are imposed on the domain of the tropical belt, $0 \leq x < 40{,}000$ km, with periodic boundary conditions in the zonal direction. The governing equations shown in Table 1 and Table 2 are solved numerically by spatially discretizing the solutions at equal-spaced grids and then temporally integrated using the 4th-order Runge-Kutta scheme. The horizontal resolution is

100 km and each time step is 4.5 min, close to typical coarse-resolution GCMs. The moisture equation with nonlinear advection terms is solved by pseudo-spectral methods. To stabilize the numerical scheme and eliminate grid-scale numerical instability, a fourth-order hyper-diffusion term is added to all prognostic equations, $-\nu f_{xxxx}$, where the dimensionless value of ν, chosen as 2×10^{-5}, is based on trial-and-error.

The radiative-convective equilibrium (RCE) state is a convenient way to describe linear convective instability of the multicloud model. Specifically, we consider a state where zonal velocity, $u=0$, and potential temperature and moisture perturbation vanish in both the troposphere and the boundary layer, $\theta_j=0, \theta_{eb}=0$ and $q=0$. The actual value of the other variables at the RCE state is included in Table 4. Both eddy momentum transfer F^u and eddy heat transfer F^θ are set to zero in the simulations presented in this section. To trigger unstable moist modes, a random field of moisture in a very weak magnitude (10^{-5} in dimensionless units) is added to the initial conditions. All solutions presented in this paper refer to the equilibrium state obtained after long simulations (4000 days in Section 2 and 3, 7000 days in Section 4).

b. Realistic MJO analog and intraseasonal variability above the equator

We first implement the 2D multicloud model with all default parameter values as in Majda et al. (2007). The default parameters for the congestus and stratiform adjustment coefficients are $\alpha_c=0.5$ and $\alpha_s=0.25$, respectively, and the background moisture stratification $\bar{Q}$ is 1.0. Although the typical value of $\bar{Q}$ in other studies based on observation has smaller value (0.9), the larger value of $\tilde{Q}$ is chosen to increase convective instability and intensify precipitation. We run the simulation for 4000 days, out of which the last 1000-day output are used in the equilibrium state for interpretation purposes. Since the model output in the default parameter regime share features that resemble observations, we regard them to be a realistic MJO analog of intraseasonal variability above the equator, and thus as a proxy for observations. It is worth clarifying that by "realistic", we refer to the good solutions with optimal parameters in this idealized framework, in contrast to the deficient solutions as shown in Sec.2c.

Fig.1a is the Hovmöller diagram for precipitation during the last 200 days, characterized by a two-scale structure consisting of eastward-moving planetary-scale envelopes and numerous embedded westward-moving synoptic-scale disturbances. The wavenumber 2 envelopes of period 40 days propagate eastward at 6.17 ms^{-1}. Embedded in these planetary-scale envelopes are several synoptic-scale disturbances that propagate westward at slower speeds, resembling the observed westward-moving superclusters in the active phases of MJO over the West Pacific, (e.g., 2-day waves (Chen et al. 1996)). However, this too-regular pulsing of precipitation during the eastward propagation of planetary-scale envelopes is less realistic than the more intermittent behavior of observed superclusters in the MJO. Fig.1b and Fig.1c show the log-scale wavenumber-frequency spectra of precipitation and zonal velocity. The eastward-moving precipitation component has a dominant peak in wavenumber 2 and period of 30 days. The spectra of zonal velocity are similar but confined to a smaller wavenumber and longer period, consistent with the observation that the dynamical circulation usually has larger spatial scales than the heating that drives it. For both precipitation and zonal velocity, the eastward-moving mode is the sum of at least three distinct harmonics with the same phase speed, thus differing from the single peak for the MJO seen in observation (Kiladis et al. 2009). The spectra of the westward-moving mode feature three regular and linear bands, according to the linearity of the dynamic core in Table 1. These multiple bands have the same slope as the three peaks of eastward-moving modes, indicating a modulation of westward-moving synoptic-scale disturbances by eastward-moving envelopes. Fig.1d-e show the zonal and vertical profiles of the composite planetary-scale envelopes in the moving frame of reference. As shown by panel (d), the precipitation peak is led by both column-integrated moisture and boundary-layer equivalent potential temperature, and followed by stratiform heating. This is consistent with the conceptual understanding that a moist free troposphere and boundary layer tends to precondition deep convection while stratiform convection in the form of anvil clouds forms subsequent to deep convection. Panel (e) shows the vertical cross-sections of zonal velocity and potential temperature anomalies in the free troposphere. Both fields are characterized by a front-to-rear tilt with increasing height, akin to the observed MJO. The surface-level westerlies resemble the WWB of the observed MJO. It is worth mentioning that the model is invariant under changing the sign of x and u so that the solution does not have direction preference. The eastward propagation of the MJO analog in Fig.1a is solely determined by the initial random perturbation.

Key features of the realistic MJO analog include the following three aspects: First, two-scale structure with eastward-moving planetary-scale envelope and embedded westward-moving synoptic-scale disturbances. Secondly, spectra of precipitation and zonal velocity with dominant peaks at wavenumber 1-3 and period of 30-90 days in eastward-moving components and wide bands of spectra signals for westward-moving components at wavenumber 5-15 and period less than 30 days. Thirdly, front-to-rear tilts in zonal velocity and potential temperature with the WWB located in the middle and west of the planetary-scale envelope. In connection with the known biases in complex weather and climate models, contemporary GCMs have difficulty in simulating the persistent eastward propagation of the MJO (Zhang 2005), let alone the embedded westward-moving synoptic-scale disturbances. Moreover, the GCMs also show significant discrepancies in the wavenumber-frequency spectra for planetary/intraseasonal variability and the WWB (Jiang et al. 2015). In the remaining experiments, we will focus on these three key features of the MJO analog.

c. Idealized GCM with clear deficiencies

Sensitivity experiments (not shown) show that the model solutions are quite sensitive to several key parameters, such as stratiform heating adjustment coefficient α_s, congestus heating adjustment coefficient α_c and background moisture stratification $\tilde{Q}$. There is no guarantee that these key parameters will have optimal values in physically motivated applications, resulting in significant bias and poor behavior. In order to mimic the behavior of GCMs with clear deficiencies, we reduce the heat adjustment coefficients for congestus α_c and stratiform convection α_s to half as shown by Table 3. Meanwhile, the background moisture stratification $\tilde{Q}$ is increased from 1.00 to 1.03 to give relatively stronger convective instability. Physically, this increment in the value of $\tilde{Q}$ corresponds to 3% more background moisture in the lower troposphere.

Fig.2a shows Hovmöller diagrams for precipitation after the system attains the equilibrium. The planetary-scale envelopes are wavenumber 4, somewhat shorter than the observed MJO wavelength in the wavenumber 1-3 range, and propagate eastward at a speed of 2.4 ms^{-1}, much slower than the typical observed MJO (5 ms^{-1}). The maximum magnitude of precipitation is equivalent to about 8 $Kday^{-1}$ heating, much weaker than in Fig.1. Fig.2b and Fig.2c show the log-scale wavenumber-frequency spectra of precipitation and zonal velocity. Notably, these spectra peaks are quasi-symmetric about the wavenumber zero axis, and both are featured by the planetary-scale (about wavenumber 4) and intraseasonal (near 40 days) variability. Such eastward/westward symmetry stems from the mixture of both eastward- and westward-moving analogs. In fact, present-day GCMs suffer a similar bias in that the spectra of westward-moving planetary-scale precipitation is as significant as its eastward-moving counterpart.

3. Upscale Impact of Mesoscale Convective Systems on the MJO Analog above the Equator

In this section, we assess the upscale impact of MCSs on the MJO analog through comparison experiments with/without eddy transfer of momentum and temperature from mesoscale fluctuations. Specifically, we use the idealized GCM with clear deficiencies in Fig.2 as the control simulation. In order to introduce the upscale impact of MCSs, we use the explicit expressions for eddy transfer of momentum and temperature obtained from theoretical predictions of the MESD model (Yang and Majda 2018b). We consider the upscale impact of MCSs that propagate either slowly (5 ms^{-1}) or rapidly ($20ms^{-1}$), either upshear or downshear, modulated by either deep heating excess or vertical shear strength. The observed typical propagation speed of MCSs lies within the range 5-20 m/s (Houze 1975, 1977, 2004). The two speeds (5 and 20 m/s) are chosen to highlight differences between slow and rapid propagating scenarios. Due to the invariance of this model under changing the signs of x, u and F^u, we only need consider the case with westward-moving MCSs because the opposite case can be inferred through counter analogy.

We investigate how the upscale impact of MCSs improves the simulations of the MJO analog in the idealized GCM with clear deficiency by conducting several experiments with different eddy transfer of momentum and temperature. In brief, we first consider cases with eddy transfer of momentum and temperature modulated by the deep heating excess in Sec.3b. Two specific cases with upscale impact of MCSs propagating westward at either a slow or fast speed are investigated. We then consider cases with eddy transfer of momentum and temperature modulated by the vertical shear strength in Sec.3c, including three cases with upscale impact of MCSs propagating westward/upshear/downshear at a slow speed are investigated. Details of the model setup in each experiment are shown in Table 5.

a. Eddy transfer of momentum and temperature predicted by the MESD model

In general, the multi-scale models based on the multi-scale asymptotic methods (Majda and Klein 2003; Majda 2007b) have been applied to study multi-scale interactions of tropical convection such as the upscale impact of synoptic-scale fluctuations on the MJO (Majda and Biello 2004; Biello and Majda 2005, 2006), the intraseasonal impact of the diurnal cycle on the MJO (Yang and Majda 2014; Majda and Yang 2016) and ITCZ breakdown (Yang et al. 2017). In particular, the Majda (2007b) MESD model has been used to assess upscale impact of embedded MCSs on eastward-moving CCKWs (Yang and Majda 2017, 2018b) and westward-moving 2-day waves (Yang and Majda 2018b). In those studies, mesoscale heating is prescribed by phase-lagged first- and second-baroclinic modes to mimic the observed front-to-rear tilt structure (Houze 2004),

$$s'_\theta = c_0 \left[\sin\left(kx' - \omega\tau\right)\sin(z) + \alpha \sin\left(kx' - \omega\tau + \phi_0\right)\sin(2z)\right] \tag{3}$$

where x' points to the propagation direction of mesoscale heating. c_0 is magnitude coefficient. k and ω are wavenumber and frequency respectively. Here α measures the relative strength of the second-baroclinic mode, and ϕ_0 the phase lag. The MESD model provides explicit expressions for eddy transfer of momentum and temperature,

$$F^u = \kappa^u \left[-\frac{3}{2}\cos(z) + \frac{3}{2}\cos(3z)\right]\cos(\gamma), \quad \kappa^u = \frac{c_0^2 \sin(\phi_0)\,\alpha k^3}{2\left(\omega^2 - k^2\right)\left(4\omega^2 - k^2\right)} \tag{4}$$

$$F^\theta = \kappa^\theta \left[\frac{3}{2}\sin(z) - \frac{9}{2}\sin(3z)\right], \quad \kappa^\theta = \frac{c_0^2 \sin(\phi_0)\,\alpha k^3 c}{2\left(\omega^2 - k^2\right)\left(4\omega^2 - k^2\right)} \tag{5}$$

where γ is the tilt angle between propagation direction of mesoscale heating and zonal direction in the horizontal plane. In the following experiments, for simplification, F^u and F^θ are further truncated by retaining only the dominant first-baroclinic mode.

Fig.3 shows vertical profiles of mesoscale fluctuations and the eddy transfer of momentum and temperature. In particular, the red curves in panels (c,d) show the corresponding eddy transfer of momentum and temperature for eastward-propagating mesoscale systems. When the mesoscale systems propagate westward, the sign of eddy momentum transfer is reversed, while that of eddy heat transfer stays the same. In fact, the CRM study by Badlan et al. (2017) showed that the vertical profile of eddy momentum transfer is dominated by the first-baroclinic mode. In the simple multicloud model that resolves the first two baroclinic modes, we further truncate the vertical profiles of eddy transfer of momentum and temperature by retaining only the first-baroclinic mode. Consequently, the eddy momentum transfer has eastward (westward) momentum forcing in the lower (upper) troposphere, with maximum strength at the surface (top) of the domain. The eddy heat transfer cools throughout the troposphere, with maximum strength in the middle troposphere.

It is straightforward to show that the ratio between F^{θ} and F^{u} in dimensionless units is determined by propagation speed of the mesoscale heating,

$$\frac{\kappa^{\theta}}{\kappa^{u}} = c \tag{6}$$

where c is the dimensionless value (dimensional value divided by 50 ms^{-1}) of propagation speed of the mesoscale heating. In the following simulations, we do not need to specify exact values of parameters in the expressions of κ^{u},κ^{θ}, but just specify the value of κ^{u}. The value of κ^{θ} is then inferred by Eq.6, when the propagation speed of the mesoscale heating c is specified.

b. Eddy transfer of momentum and temperature modulated by deep heating excess

Here we consider the scenario when the eddy transfer of momentum and temperature in the first baroclinic mode is modulated by the maximum allowable deep heating excess P_0 as follows,

$$F^{u} = \kappa^{u}\frac{P_0^{+}}{\bar{Q}}\left[-\frac{3}{2}\cos(z)\right] \tag{7}$$

$$F^{\theta} = \kappa^{\theta}\frac{P_0^{+}}{\bar{Q}}\left[\frac{3}{2}\sin(z)\right] \tag{8}$$

where $P_0 = \frac{1}{\tau_{conv}} \left(a_1 \theta_{eb} + a_2 q - a_0 \left(\theta_1 + \gamma_2 \theta_2 \right) \right)$ is the anomaly component of the maximum allowable deep heating (see Table 2). $\bar{Q}$ is the corresponding RCE value. The value of the expression P_0^+ stays the same as P_0 if P_0 is positive and zero if it is negative. The closure for P_0 is a combination of the Betts-Miller relaxation-type parameterization and convective available potential energy (CAPE) parameterization. Physically, the maximum allowable deep heating excess P_0 resembles the effect of CAPE in modulating MCSs and the resulting CMT (Moncrieff 2004). Majda and Stechmann (2008) developed a stochastic parameterization for CMT, whose strength is modulated by the square of the maximum allowable deep heating.

Three cases are compared with/without F^u and F^θ modulated by the effects of P_0. The first case is the control simulation in Fig.2. The second and third cases consider the eddy transfer of momentum and temperature from MCSs that propagate at a slow (5 ms^{-1}) and fast speed (20 ms^{-1}). The magnitude coefficient for eddy momentum transfer κ^u is fixed at 0.0032. The difference between the second and third cases lies in the stronger magnitude of F^θ in the case of fast propagation.

Fig.4 shows the Hovmöller diagrams for precipitation. The control simulation in Fig.4a features both eastward- and westward-moving planetary-scale disturbances with no clear two-scale structure. Compared with the control simulation, the cases with eddy terms in panels b and c show an apparent two-scale structure, where planetary-scale envelopes propagate eastward and embedded synoptic-scale disturbances propagate westward. In panel b, the maximum magnitude of precipitation is equivalent to 28 K/day. Such intense precipitation and the promoted eastward-moving planetary-scale envelope by westward-moving MCSs is consistent with Yang and Majda (2018b). In panel c, the maximum magnitude of precipitation is reduced to 12 K/day and convection is suppressed due to the extra cooling from eddy heat transfer, again consistent with Yang and Majda (2018b). This extra cooling reduces low-level moisture convergence, resulting in a weaker growth rate of the unstable modes.

Fig.5 shows the log-scale wavenumber-frequency spectra of precipitation and zonal velocity. Compared with the control simulation in panel a, both cases show a clear east/west contrast in the spectra, similar to the realistic MJO analog shown in Fig.1. For the slowly propagating MCSs, the spectra of precipitation in panel c are characterized by three discrete spectra peaks for the eastward-moving components and three bands of spectra of westward-moving components. In particular, the peak for eastward-moving planetary-scale envelope has wavenumber 3 and period about 50 days. The spectra of zonal velocity in panel d resembles that in panel c, indicating close correlation between convection and the large-scale circulation. As for the faster propagating MCSs in panels e-f, the associated spectra of precipitation are dominated by a planetary-scale peak for the eastward-moving component and a band of spectra for the westward-moving component.

Fig.6 shows the vertical cross-sections of the composite planetary-scale envelopes in the moving reference frame. The vertical structure of zonal velocity and potential temperature anomalies features a significant front-to-rear tilt, consistent with the built-in transition of life-cycle from congestus to deep to stratiform convection. In panel a, the maximum magnitude of zonal velocity of about 2 ms^{-1} is at the top of the domain. In the lower troposphere, the wind convergence is mostly in phase with the maximum precipitation with westerlies to the west and easterlies to the east. The WWB is negligible. The maximum magnitude of both positive and negative potential temperature are both attained in the upper troposphere. In contrast, both the maximum magnitude of zonal velocity, potential temperature anomalies and precipitation anomalies in panel b are much weaker than those in panel a, indicating suppressed convection due to eddy heat transfer. The control simulation features a mixture of both eastward- and westward-propagating large-scale disturbances. The corresponding composite planetary-scale envelope that is calculated only along the eastward-moving reference frame is less meaningful and thus not shown.

c. Eddy transfer of momentum and temperature modulated by vertical shear

Here we consider the scenario when eddy transfer of momentum and temperature is modulated by the strength of vertical shear $\triangle U$ as follows,

$$F^u = \kappa^u \frac{\triangle U}{U_{ref}} \left[-\frac{3}{2} \cos(z) \right] \tag{9}$$

$$F^\theta = \kappa^\theta \frac{\triangle U}{U_{ref}} \left[\frac{3}{2} \sin(z) \right] \tag{10}$$

where $U_{ref} = 50ms^{-1}$ and the strength of vertical shear is defined as follows,

$$U^u_{max} = \max_{\pi/2 \le z \le \pi} \{u\} ; U^u_{min} = \min_{\pi/2 \le z \le \pi} \{u\} \tag{11}$$

$$U^l_{max} = \max_{0 \le z \le \pi/2} \{u\} ; U^l_{min} = \min_{0 \le z \le \pi/2} \{u\} \tag{12}$$

$$\triangle U \equiv max \left\{ \left| U^u_{max} - U^l_{min} \right|, \left| U^u_{min} - U^l_{max} \right| \right\} \tag{13}$$

Fig.7a explains the definition of vertical shear strength U^l_{max}, which basically calculates the maximum possible easterly and westerly shear between the upper and lower troposphere and selects the larger one. Fig.7b describes the scenarios when the MCSs propagate upshear (along the opposite direction of vertical shear) and downshear (along the same direction of vertical shear).

Four cases are compared with/without F^u and F^θ modulated by the effects of $\triangle U$. Besides the first cases from the control simulation in Fig.2, the remaining three cases consider the eddy transfer of momentum and temperature from MCSs that propagate westward, upshear and downshear at a slow speed (5 ms^{-1}). Correspondingly, the magnitude coefficient of eddy momentum transfer κ^u is 0.0024, 0.0030, 0.0030, respectively. The choice of a smaller value of κ^u in the second case is to obtain a more realistic precipitation intensity.

Fig.8 shows the Hovmöller diagrams for precipitation. Compared with the control simulation in Fig.8a, the maximum magnitude of precipitation in both Fig.8b and Fig.8c is intensified, while that in Fig.8d is weakened. Specifically, the maximum magnitude of precipitation in Fig.8b reaches

25 K/day, consistent with the Yang and Majda (2018b) result that westward-moving MCSs favor the eastward propagation of convection. The pattern of spatio-temporal variability of precipitation in Fig.8b features the two-scale structure with eastward-moving planetary-scale envelopes at wavenumber 3 and embedded shorter wavelength westward-moving synoptic-scale disturbances. Compared with the realistic MJO analog in Fig.1, the solutions exhibit more intermittency in precipitation intensity and spatio-temporal pattern. In Fig.8c, the maximum precipitation also intensifies to 19 K/day, which is associated with the strengthened low-level moisture convergence due to the positive feedback between vertical shear and eddy momentum transfer. The precipitation anomalies are dominated by both eastward- and westward-moving planetary-scale envelopes and exhibit no clear east/west contrast. Based on a similar argument, the precipitation in Fig.8d is reduced due to the negative feedback between vertical shear and eddy momentum transfer from downshear-moving MCSs. Due to the lack of persistent propagating planetary-scale envelopes, this downshear-moving case is omitted in Fig.9 and Fig.10.

Fig.9 shows the log-scale wavenumber-frequency spectra of precipitation and zonal velocity for these three cases. Compared with the symmetric spectra in the control simulation, Fig.9c and Fig.9d are characterized by significant zonal asymmetry. Specifically, the eastward-moving components are dominated by a continuous band of spectra along the non-dispersive line across the equator, which extends from wavenumber 3 to 10 and period from 15 days to 50 days. In this case, such continuous spectra reflect the intermittent nature of both precipitation and zonal velocity. For the case in Fig.9e and Fig.9f, the spectra of both precipitation and zonal velocity exhibits significant symmetry under changing sign of x, indicating the prevalence of both the eastward-moving MJO analog and westward-moving reversed MJO analog.

Fig.10 shows vertical cross-sections of zonal velocity and potential temperature anomalies. Notably, the WWB does not reach the surface in Fig.10a, whereas it has a much stronger magnitude in

Fig.10b. In the case with eddy terms from westward-moving MCSs, the eddy momentum transfer induces low-level westward (upper-level eastward) momentum forcing, reducing the westerlies to the west but increasing easterlies to the east. In contrast, in the case where MCSs propagate upshear, the positive feedback between vertical shear and eddy momentum transfer tends to strengthen both westerlies (easterlies) to the west (east) at the surface (see Eq.9). Due to the relatively stronger modulation by vertical shear strength to the west, the resulting surface-level westerly winds dominate. In these two cases, both zonal velocity and potential temperature fields exhibit a front-to-rear tilt, due to the built-in transition from congestus to deep to stratiform convection.

4. Parameterization of the Upscale Impact of MCSs in the Idealized GCM

According to Section 3, the upscale impact of westward-moving MCSs under the modulation of deep heating excess produces a persistent propagating MJO analog with a two-scale structure and realistic variability of precipitation and winds. In contrast, the upscale impact of upshear-moving MCSs under the modulation of vertical shear strength produces a significant WWB. In this section, we provide a basic parameterization of the upscale impact of upshear-moving MCSs modulated by both deep heating excess and vertical shear strength. We test the improvement of key features of the MJO analog in the idealized GCM having clear deficiencies. In particular, we focus on the cases with upscale impact of MCSs propagating upshear at a slow speed, modulated by the effects of both deep heating excess and vertical shear strength.

a. A basic parameterization of upscale impact of MCSs combining upshear momentum and deep heating excess in the GCM

In reality, the maximum allowable deep heating P_0 (conceptually similar to CAPE) should mainly influence the magnitude of mesoscale heating, while the vertical shear strength influences the vertical tilting angles of MCSs (i.e., relative location among shallow congestus, deep and stratiform convection). According to previous results based on the MESD model (Yang and Majda 2018b), both conditions control the magnitude and sign of the eddy transfer of momentum and temperature. Here we combine these two conditions by summing them linearly with a tuning coefficient α, and assume that the MCSs all propagate upshear.

A basic parameterization for upscale impact of MCSs (eddy transfer of momentum and temperature F^u, F^θ) is,

$$F^u = \kappa^u \left(\alpha \frac{P_0}{\bar{Q}} + (1-\alpha) \frac{|\triangle U|}{U_{ref}} \right) sign\left(\triangle U\right) \left[-\frac{3}{2} \cos\left(z\right) \right] \tag{14}$$

$$F^\theta = \kappa^\theta \left(\alpha \frac{P_0}{\bar{Q}} + (1-\alpha) \frac{|\triangle U|}{U_{ref}} \right) \left[\frac{3}{2} \sin\left(z\right) \right] \tag{15}$$

where $P_0 = \left| \frac{1}{\tau_{conv}} \left(a_1 \theta_{eb} + a_2 q - a_0 \left(\theta_1 + \gamma_2 \theta_2 \right) \right) \right|^+$ is the positive excess of the maximum allowable deep heating and $\bar{Q}$ is its RCE value, and $\triangle U$ represents the vertical shear strength, $U_{ref} = 10 ms^{-1}$. Recall that the magnitude coefficients $\kappa^u > 0, \kappa^\theta < 0$ satisfy the relation $\left| \frac{\kappa^\theta}{\kappa^u} \right| = c$, where c is the absolute propagation speed of the MCSs. The coefficient α controls the relative importance of P_0 and vertical shear strength in modulating the strength of the eddy transfer of momentum and temperature.

b. Three-way interaction between MJO analog, parameterized upscale impact of MCSs, and background vertical shear on longer time scales

Here we test effects of the parameterization by adding it into the idealized GCM having clear deficiencies. Four cases with various value of α in Eqs.14-15 are considered. The magnitude coefficient κ^u is fixed at 0.0008 and speed of MCSs c is 0.1 (corresponds to 5 ms^{-1}). In order to explore the solutions over longer time scales, we extend the integration period to 7000 days and use the last 3000-day model output for analysis. For better visualization, we perform a low-pass filtering by transforming solutions into wavenumber-frequency spectra in Fourier space and only keeping small wavenumber and frequency (large wavelength and period). Only precipitation anomalies at the length scale longer than 10,000 km and time scale longer than 30 days are retained.

Fig.11 shows the Hovmöller diagrams for precipitation with various value of α. A large value of α corresponds to stronger modulation by deep heating excess P_0, while a smaller value of α corresponds to stronger modulation by vertical shear strength. One particular interesting feature is the direction switching of the MJO analog for $\alpha = 0.8$ (panel c) and $\alpha = 1.0$ (panel d). In panel c, the MJO analog persistently propagates eastward between day 4000 and day 4500, switches to westward propagation between day 4500 and day 4800, then switches back to eastward propagation between day 5000 and day 5300, and so forth. The period between two eastward (or westward) propagation phases is about 800 days, much longer than the intraseasonal time scale. Such a QBO-like behavior in the presence of CMT are quite similar to Majda and Stechmann (2009) which also shows periodic direction switching of unstable CCEWs and background mean flow. It is worth clarifying that by "QBO-like", we mean the behavior of direction switching is similar to the manifestation of the QBO but not the underlying processes. Compared with panel c, the solution in panel d differs in the duration of persistent propagation of the MJO analog/reversed MJO analog in each phase, exhibiting more chaotic features. For example, the persistently eastward-propagating MJO analog lasts 1200 days between day 5500 and day 6700, while that between day 4500 and day 5000 only last 500 days. Unlike panels c and d, the solutions in panels a and b show little QBO-like behavior. Such a clear difference among the cases with large/small value of α indicates the crucial modulation effects of deep heating excess on the eddy terms from upshear-moving MCSs. As shown by Fig.11e, the realistic MJO analog features persistent eastward propagation over a long time period. In contrast, the solution in Fig.11f from the deficient GCM shows a transient behavior with alternate eastward/westward propagation during day 4000 and day 5000, standing-wave pattern near day 5500 and persistent westward propagation after day 6000.

For $\alpha = 0.8$ in Fig.12a shows a periodic direction-switch between eastward-propagating MJO analog and westward-propagating reversed MJO analog. Panel b shows the domain-mean zonal winds in the first-baroclinic mode, which also exhibits a periodic direction-switch between easterlies and westerlies. Such a QBO-like behavior in domain-mean flow also occurs in the CRM studies by Held et al. (1993). Specifically, during the phase with eastward-moving (westward-moving) MJO analog, the domain-mean zonal winds gradually increase from low-level easterlies (westerlies) to low-level westerlies (easterlies), reaching its maximum magnitude as the MJO analog switches direction. The persistently eastward (westward) propagation phase is highly correlated with the increasing (decreasing) background zonal winds. According to the governing equations for u_1 in Table 1, domain-mean zonal winds vanish in the cases without eddy momentum transfer. Thus, the accumulating contribution by eddy momentum transfer modulated by deep heating excess associated with the MJO analog induces these nonzero domain-mean background flow. Fig.12c shows the time series of domain-mean thermodynamical fields, including first-baroclinic potential temperature, boundary-layer equivalent potential temperature, and moisture. The domain-mean first-baroclinic potential temperature decreases at each phase when MJO analog persistently propagates westward/eastward. Such cooling effects can be explained by eddy heat transfer from MCSs that accumulate in space and time as the MJO analog persistently propagates across the domain.

Fig.13a shows the zonal/vertical cross-sections of zonal velocity and zonal profiles of deep heating excess and vertical shear strength in the composite eastward-moving planetary-scale envelopes. A significant WWB is produced, resembling the realistic MJO analog in Fig.1. A crucial feature is the displacement of the peak of deep heating excess to the west of the dashed line, which is consistent with the observation that convective center of the MJO typically sits over the WWB in easterly vertical shear. Such westward displacement of the deep heating excess preferably modulates eddy momentum transfer in the trailing edge, resulting in a stronger low-level eastward momentum forcing in the trailing edge than in the leading edge. The relatively weak maximum zonal velocity compared to the realistic MJO analog in Fig.1 is due to the intermittent property of the solutions shown in the Hovmöller diagram in Fig.13b. Specifically, westerlies and easterlies are not aligned during the eastward propagation of planetary-scale envelopes and cancel each other after averaging in the eastward-moving reference frame.

We identify the following three-way interaction between MJO analog, parameterized upscale impact of MCSs, and background vertical shear:

1. Eastward-moving MJO analog modulates eddy momentum transfer mainly through deep heating excess.

2. Due to the westward displacement of the deep heating excess, the resulting eddy momentum transfer with low-level eastward momentum forcing accumulates in space and time and switches the low-level background flow from easterlies to westerlies. This explains why the propagation direction of the MJO analog matches that of the change in background winds.

3. Background vertical shear with low-level westerlies favors the westward-moving reversed MJO analog. The underlying mechanism is related to eastward moisture advection, resulting in eastward-moving synoptic-scale disturbances and a westward-moving planetary-scale envelope. This explains why the background winds peaks slightly lead the direction switching of the MJO analog.

4. Mechanisms similar to 1-3 are repeated, but in opposite directions.

Fig.13c-d shows the log-scale wavenumber-frequency spectra of precipitation and zonal velocity, which is akin to the realistic MJO analog in Fig.1. The spectra of both fields show a clear peak for eastward-moving planetary-scale envelope at wavenumber 2 and period of 50 days, with a band of extra spectra extending to higher wavenumber and frequency. For westward-moving components, the spectra of precipitation shows a peak at wavenumber 5-8 and period of 25-40 days. Extra bands of spectra occur at higher wavenumber and frequency, while that of zonal velocity has a more dominant peak at smaller wavenumber.

It is interesting to question why the scenario with dominant modulation effects by vertical shear does not exhibit such a QBO-like behavior, considering that the easterly vertical shear in the trailing edge is stronger than in the leading edge. Although the magnitude of westerly vertical shear in the leading edge is weaker, it covers a much broader area. After the eddy momentum transfer in both leading and trailing edges accumulate in space, the resulting background zonal winds are comparable with no persistent direction preference. Also, the mechanism that background vertical shear with low-level westerlies favoring westward-moving reversed MJO analog differs from the observation over Indian Ocean, presumably due to the idealized two-dimensional model setup without rotation. In the three-dimensional model setup, the presence of the Coriolis force would break the zonal symmetry and induce favorable propagation direction of the MJO analog.

c. Improving other deficiencies by parameterizing the upscale impact of MCSs

It would be interesting to consider other deficiencies in this idealized GCM due to different parameter values and investigate how the upscale impact of MCSs would improve them. Here we specifically focus on two deficiencies. The first one has almost the same parameters as the realistic simulation in Fig.1, except for the coefficient of the second-baroclinic mode in linear moisture convergence $\tilde{\lambda} = 0.3$ (optimal value is 0.6) and the background moisture stratification $\tilde{Q} = 1.03$ (optimal value is 1.0). This deficiency due to the reduced coupling of the second-baroclinic mode mimics the underestimated role of shallow convection in the cumulus parameterization in the GCMs (Zhang and Song 2009). The second deficiency differs from the realistic simulation in Fig.1 only by the inverse convective buoyancy time scale of deep clouds $a_0 = 32$ (optimal value is 12). These two deficiencies are modified by adding the parameterization under the same configuration as Fig.13.

Fig.14a shows the Hovmöller diagram for precipitation in the first deficiency during a 200-day period. The solution is characterized by eastward-moving precipitating events in wavenumber 5 and period of 40 days. In contrast, the improved simulation by the parameterization in Fig.14b shows a clear two-scale structure with eastward-moving planetary-scale envelopes and embedded westward-moving synoptic-scale disturbances. The maximum precipitation is intensified to 30 $Kday^{-1}$. Over a longer period, this improved simulation also shows a QBO-like behavior with direction switching in Fig.14c, similar to Fig.12a. Fig.14d shows the Hovmöller diagram for precipitation in the second deficiency. The solution is characterized by periodic eastward-moving events in wavenumber 5, which has much shorter length scale than the observed MJO in wavenumber 1-3 (Kiladis et al. 2009). After adding the parameterization, these eastward-moving events have larger spatial scales in wavenumber 3 with more intermittency in Fig.14e. Interestingly, these planetary-scale envelopes exhibit persistent eastward propagation over the longer period in Fig.14f, presumably due to the stronger coupling with the second-baroclinic mode.

5. Concluding Discussion

A simple multicloud model for MJO analog and intraseasonal variability above the equator is studied. With reduced congestus and stratiform heating, the resulting solutions from this simple model are used as an idealized GCM having clear deficiencies. By adding eddy transfer of momentum and temperature predicted by the MESD model, we assess the upscale impact of MCSs on three key features of the MJO analog: persistent propagation of a two-scale structure, realistic planetary/intraseasonal variability in precipitation and winds, and a significant WWB. We then introduce a basic parameterization of upscale impact of upshear-moving MCSs modulated by the effects of deep heating excess and vertical shear strength and test its effects in the idealized deficient GCM.

Table 5 summarizes results reported in this paper regarding the above three key features of the MJO analog in the idealized deficient GCM. Compared to the realistic MJO analog, the idealized deficient GCM fails to reproduce these three features, thereby mimicking the significant bias of the simulated MJO in present-day GCMs. According to Khouider et al. (2012), MCSs and squall lines are prominent in the convectively active regions of the MJO envelope, indicating the modulation of the MCSs by the MJO convective center. The eddy transfer of momentum and temperature from westward-moving MCSs traveling at a slow speed (5 ms^{-1}) improves the two-scale structure of the eastward-moving MJO analog and space-time variability of precipitation and winds, but fails to strengthen WWB. This is consistent with the theoretical prediction by the MESD model (Yang and Majda 2018b); i.e., westward-moving MCSs embedded in the large-scale convective envelope provide favorable conditions for convection to the east, that promotes the eastward-moving convective envelope. On the other hand, vertical shear plays a crucial role in organized tropical convection (Moncrieff 1992), including the influence on its front-to-rear tilt structure and propagation directions (Moncrieff and Liu 1999; Stechmann and Majda 2009). In particular, eddy transfer of momentum and temperature from upshear-moving MCSs induces a significant WWB in the middle and west of the MJO analog. This is due to the two-way feedback between environmental easterly vertical shear and the embedded eddy momentum transfer with low-level eastward momentum forcing. The eddy transfer of momentum and temperature modulated by the effects of vertical shear strength alone fails to reproduce the two-scale structure of the MJO analog and a realistic space-time variability of precipitation and winds.

In order to incorporate those improvements in global models, we provide a basic parameterization of the upscale impact of upshear-moving MCSs that linearly combines the modulation effects of deep heating excess and vertical shear strength. This basic parameterization shares goals similar to the MCSP introduced by Moncrieff et al. (2017); notably representing the upscale effects of organized tropical convection that are missing from contemporary parameterizations in GCMs. The main purpose of the Moncrieff et al. (2017) prototype version of MCSP was to demonstrate the upscale effects of top-heavy convective heating and momentum transport in the simplest possible manner, in order to provide proof-of-concept. This was achieved by focusing on eastward propagation and a full GCM. The results of this present paper will be valuable for the future development of MCSP, because the heating and CMT (i.e., upscale impact of MCSs) have been quantified in simplest ways. However, this basic parameterization differs from the MCSP in several aspects that significantly improve the feasibility and reliability of the parameterization. First, it considers both deep heating excess (a similar concept as CAPE) and vertical shear strength in modulating the upscale impact of MCSs, while the parameterized CMT in MCSP has constant magnitude over convective regions. Secondly, it assumes eddy transfer of momentum and temperature from MCSs that propagate upshear (opposite to vertical shear direction), allowing vertical shear to determine the propagation direction of MCSs and the sign of eddy momentum transfer. Thirdly, it highlights the crucial contribution of eddy transfer of temperature as predicted theoretically by the MESD model.

The implementation of this basic parameterization of upscale impact of MCSs in the idealized deficient GCM shows significant improvement in capturing key features of the MJO. A further examination of a longer-period simulation reveals a three-way interaction between the MJO analog, the parameterization of upscale impact of MCSs, and the background mean flow. The westward-displaced deep heating excess in the eastward-moving MJO analog favors eddy momentum transfer with low-level eastward (upper-level westward) momentum forcing. The effects of the eddy momentum transfer accumulate in space and time and gradually switches the direction of background mean flow which, in turn, alter the propagation directions of the MJO analog. Under this three-way interaction mechanism, the background mean flow exhibits a QBO-like behavior, resembling similar phenomenon in CRM simulations (Held et al. 1993). Although in reality the Coriolis force would break down the zonal symmetry, such a three-way interaction mechanism may shed light on the interactions between eastward-moving MJO, upscale impact of MCSs and climatological vertical shear.

The basic parameterization of upscale impact of MCSs can be elaborated in several ways and tested in a hierarchy of models. Besides the first-baroclinic mode, it is also interesting to investigate the effects of eddy transfer of momentum and temperature due to higher baroclinic modes, as shown by studies based on the MESD model (Yang and Majda 2018b) and reanalysis data (Oh et al. 2015). A different scenario to assess the upscale impact of MCSs on the planetary/intraseasonal variability includes the Walker circulation over the warm pool. Furthermore, we would like to test effects of this basic parameterization of upscale impact of MCSs in more comprehensive GCMs.

Acknowledgments. This research of A.J.M. is partially supported by the office of Naval Research ONR MURI N00014-12-1-0912 and the Center for Prototype Climate Modeling (CPCM) in New York University Abu Dhabi (NYUAD) Research Institute. Q.Y. is funded as a postdoctoral fellow by CPCM in NYUAD Research Institute. NCAR is sponsored by the National Science Foundation.

References

Badlan, R. L., T. P. Lane, M. W. Moncrieff, and C. Jakob, 2017: Insights into convective momentum transport and its parametrization from idealized simulations of organized convection. *Quart. J. Roy. Meteor. Soc.*, **143 (708)**, 2687–2702.

Biello, J. A., and A. J. Majda, 2005: A new multiscale model for the Madden-Julian oscillation. *J. Atmos. Sci.*, **62 (6)**, 1694–1721.

Biello, J. A., and A. J. Majda, 2006: Modulating synoptic scale convective activity and boundary layer dissipation in the IPESD models of the Madden–Julian oscillation. *Dyn. Atmos. Oceans*, **42 (1)**, 152–215.

Brenowitz, N., A. Majda, and Q. Yang, 2018: The multiscale impacts of organized convection in global 2-d cloud-resolving models. *JAMES*, **10 (8)**, 2009–2025.

Chen, S. S., R. A. Houze, Jr., and B. E. Mapes, 1996: Multiscale variability of deep convection in realation to large-scale circulation in TOGA COARE. *J. Atmos. Sci.*, **53 (10)**, 1380–1409.

Del Genio, A. D., Y. Chen, D. Kim, and M.-S. Yao, 2012: The MJO transition from shallow to deep convection in cloudsat/calipso data and giss gcm simulations. *J. Climate*, **25 (11)**, 3755–3770.

Del Genio, A. D., J. Wu, A. B. Wolf, Y. Chen, M.-S. Yao, and D. Kim, 2015: Constraints on cumulus parameterization from simulations of observed MJO events. *J. Climate*, **28 (16)**, 6419–6442.

Deng, Q., B. Khouider, and A. J. Majda, 2015: The MJO in a coarse-resolution gcm with a stochastic multicloud parameterization. *J. Atmos. Sci.*, **72 (1)**, 55–74.

Frenkel, Y., B. Khouider, and A. J. Majda, 2011a: Simple multicloud models for the diurnal cycle of tropical precipitation. part i: Formulation and the case of the tropical oceans. *J. Atmos. Sci.*, **68 (10)**, 2169–2190.

Frenkel, Y., B. Khouider, and A. J. Majda, 2011b: Simple multicloud models for the diurnal cycle of tropical precipitation. part ii: The continental regime. *J. Atmos. Sci.*, **68 (10)**, 2192–2207.

Frenkel, Y., A. J. Majda, and B. Khouider, 2013: Simple models for the diurnal cycle and convectively coupled waves. *Theor. Comput. Fluid Dyn.*, **27 (3-4)**, 533–559.

Goswami, B., B. Khouider, R. Phani, P. Mukhopadhyay, and A. J. Majda, 2017: Improving synoptic and intra-seasonal variability in CFSv2 via stochastic representation of organized convection. *Geophys. Res. Lett.*, **44 (2)**, 1104–1113.

Grabowski, W. W., 2001: Coupling cloud processes with the large-scale dynamics using the cloud-resolving convection parameterization (CRCP). *J. Atmos. Sci.*, **58 (9)**, 978–997.

Grabowski, W. W., 2003: MJO-like systems and moisture-convection feedback in idealized aqua-planet simulations. *Proc. Workshop on Simulation and Prediction of Intraseasonal Variability with Emphasis on the MJO*, 67–72.

Grabowski, W. W., 2004: An improved framework for superparameterization. *J. Atmos. Sci.*, **61 (15)**, 1940–1952.

Grabowski, W. W., and M. W. Moncrieff, 2001: Large-scale organization of tropical convection in two-dimensional explicit numerical simulations. *Quart. J. Roy. Meteor. Soc.*, **127 (572)**, 445–468.

Harlim, J., and A. J. Majda, 2013: Test models for filtering and prediction of moisture-coupled tropical waves. *Quart. J. Roy. Meteor. Soc.*, **139 (670)**, 119–136.

Held, I. M., R. S. Hemler, and V. Ramaswamy, 1993: Radiative-convective equilibrium with explicit two-dimensional moist convection. *J. Atmos. Sci.*, **50 (23)**, 3909–3927.

Henderson, S. A., E. D. Maloney, and S.-W. Son, 2017: Madden–Julian oscillation pacific teleconnections: The impact of the basic state and MJO representation in general circulation models. *J. Climate*, **30 (12)**, 4567–4587.

Horinouchi, T., and S. Yoden, 1998: Wave–mean flow interaction associated with a QBO-like oscillation simulated in a simplified gcm. *J. Atmos. Sci.*, **55 (4)**, 502–526.

Houze, R. A., Jr., 1975: Squall lines observed in the vicinity of the researcher during phase III of GATE. *Preprints, 16th Radar Meteorology Conf., Houston, TX, American Meteorological Society*, 206–209.

Houze, R. A., Jr., 1977: Structure and dynamics of a tropical squall-line system. *Mon. Wea. Rev.*, **105 (12)**, 1540–1567.

Houze, R. A., Jr., 2004: Mesoscale convective systems. *Rev. Geophys.*, **42 (4)**.

Houze Jr, R. A., S. S. Chen, D. E. Kingsmill, Y. Serra, and S. E. Yuter, 2000: Convection over the pacific warm pool in relation to the atmospheric kelvin-rossby wave. *J. Atmos. Sci.*, **57 (18)**, 3058–3089.

Jiang, X., and Coauthors, 2015: Vertical structure and physical processes of the Madden-Julian oscillation: Exploring key model physics in climate simulations. *Journal of Geophysical Research: Atmospheres*, **120 (10)**, 4718–4748.

Johnson, R. H., T. M. Rickenbach, S. A. Rutledge, P. E. Ciesielski, and W. H. Schubert, 1999: Trimodal characteristics of tropical convection. *J. Climate*, **12 (8)**, 2397–2418.

Khouider, B., J. Biello, and A. J. Majda, 2010: A stochastic multicloud model for tropical convection. *Communications in Mathematical Sciences*, **8 (1)**, 187–216.

Khouider, B., Y. Han, A. J. Majda, and S. N. Stechmann, 2012: Multiscale waves in an MJO background and convective momentum transport feedback. *J. Atmos. Sci.*, **69 (3)**, 915–933.

Khouider, B., and A. J. Majda, 2006a: Model multi-cloud parameterizations for convectively coupled waves: Detailed nonlinear wave evolution. *Dyn. Atmos. Oceans*, **42 (1)**, 59–80.

Khouider, B., and A. J. Majda, 2006b: Multicloud convective parametrizations with crude vertical structure. *Theor. Comput. Fluid Dyn.*, **20 (5-6)**, 351–375.

Khouider, B., and A. J. Majda, 2006c: A simple multicloud parameterization for convectively coupled tropical waves. part I: Linear analysis. *J. Atmos. Sci.*, **63 (4)**, 1308–1323.

Khouider, B., and A. J. Majda, 2007: A simple multicloud parameterization for convectively coupled tropical waves. part II: Nonlinear simulations. *J. Atmos. Sci.*, **64 (2)**, 381–400.

Khouider, B., and A. J. Majda, 2008a: Equatorial convectively coupled waves in a simple multicloud model. *J. Atmos. Sci.*, **65 (11)**, 3376–3397.

Khouider, B., and A. J. Majda, 2008b: Multicloud models for organized tropical convection: Enhanced congestus heating. *J. Atmos. Sci.*, **65 (3)**, 895–914.

Kiladis, G. N., M. C. Wheeler, P. T. Haertel, K. H. Straub, and P. E. Roundy, 2009: Convectively coupled equatorial waves. *Rev. Geophys.*, **47 (2)**.

Lappen, C.-L., and C. Schumacher, 2012: Heating in the tropical atmosphere: what level of detail is critical for accurate MJO simulations in gcms? *Climate Dyn.*, **39 (9-10)**, 2547–2568.

LeMone, M. A., 1983: Momentum transport by a line of cumulonimbus. *J. Atmos. Sci.*, **40 (7)**, 1815–1834.

LeMone, M. A., and M. W. Moncrieff, 1994: Momentum and mass transport by convective bands: Comparisons of highly idealized dynamical models to observations. *J. Atmos. Sci.*, **51 (2)**, 281–305.

LeMone, M. A., E. J. Zipser, and S. B. Trier, 1998: The role of environmental shear and thermodynamic conditions in determining the structure and evolution of mesoscale convective systems during TOGA COARE. *J. Atmos. Sci.*, **55 (23)**, 3493–3518.

Lin, X., and R. H. Johnson, 1996: Kinematic and thermodynamic characteristics of the flow over the western pacific warm pool during TOGA COARE. *J. Atmos. Sci.*, **53 (5)**, 695–715.

Majda, A. J., 2007a: Multiscale models with moisture and systematic strategies for superparameterization. *J. Atmos. Sci.*, **64 (7)**, 2726–2734.

Majda, A. J., 2007b: New multiscale models and self-similarity in tropical convection. *J. Atmos. Sci.*, **64 (4)**, 1393–1404.

Majda, A. J., and J. A. Biello, 2004: A multiscale model for tropical intraseasonal oscillations. *Proc. Natl. Acad. Sci. (USA)*, **101 (14)**, 4736–4741.

Majda, A. J., and R. Klein, 2003: Systematic multiscale models for the tropics. *J. Atmos. Sci.*, **60 (2)**, 393–408.

Majda, A. J., and S. N. Stechmann, 2008: Stochastic models for convective momentum transport. *Proc. Natl. Acad. Sci. (USA)*, **105 (46)**, 17 614–17 619.

Majda, A. J., and S. N. Stechmann, 2009: A simple dynamical model with features of convective momentum transport. *J. Atmos. Sci.*, **66 (2)**, 373–392.

Majda, A. J., S. N. Stechmann, and B. Khouider, 2007: Madden–Julian oscillation analog and intraseasonal variability in a multicloud model above the equator. *Proc. Natl. Acad. Sci. (USA)*, **104 (24)**, 9919–9924.

Majda, A. J., and Q. Yang, 2016: A multiscale model for the intraseasonal impact of the diurnal cycle over the maritime continent on the Madden–Julian oscillation. *J. Atmos. Sci.*, **73 (2)**, 579–604.

Miura, H., M. Satoh, T. Nasuno, A. T. Noda, and K. Oouchi, 2007: A Madden-Julian oscillation event realistically simulated by a global cloud-resolving model. *Science*, **318 (5857)**, 1763–1765.

Moncrieff, M., 1981: A theory of organized steady convection and its transport properties. *Quart. J. Roy. Meteor. Soc.*, **107**, 29–50.

Moncrieff, M. W., 1992: Organized convective systems: Archetypal dynamical models, mass and momentum flux theory, and parametrization. *Quart. J. Roy. Meteor. Soc.*, **118 (507)**, 819–850.

Moncrieff, M. W., 2004: Analytic representation of the large-scale organization of tropical convection. *J. Atmos. Sci.*, **61 (13)**, 1521–1538.

Moncrieff, M. W., and E. Klinker, 1997: Organized convective systems in the tropical western pacific as a process in general circulation models: A TOGA COARE case-study. *Quart. J. Roy. Meteor. Soc.*, **123 (540)**, 805–827.

Moncrieff, M. W., and C. Liu, 1999: Convection initiation by density currents: Role of convergence, shear, and dynamical organization. *Mon. Wea. Rev.*, **127 (10)**, 2455–2464.

Moncrieff, M. W., C. Liu, and P. Bogenschutz, 2017: Simulation, modeling, and dynamically based parameterization of organized tropical convection for global climate models. *J. Atmos. Sci.*, **74 (5)**, 1363–1380.

Nakazawa, T., 1988: Tropical super clusters within intraseasonal variations over the western pacific. *J. Meteor. Soc. Japan*, **66 (6)**, 823–839.

Nishimoto, E., S. Yoden, and H.-H. Bui, 2016: Vertical momentum transports associated with moist convection and gravity waves in a minimal model of QBO-like oscillation. *J. Atmos. Sci.*, **73 (7)**, 2935–2957.

Oh, J.-H., X. Jiang, D. E. Waliser, M. W. Moncrieff, and R. H. Johnson, 2015: Convective momentum transport associated with the Madden–Julian oscillation based on a reanalysis dataset. *J. Climate*, **28 (14)**, 5763–5782.

Randall, D., M. Khairoutdinov, A. Arakawa, and W. Grabowski, 2003: Breaking the cloud parameterization deadlock. *Bull. Amer. Meteor. Soc.*, **84 (11)**, 1547–1564.

Seo, K.-H., and W. Wang, 2010: The Madden–Julian oscillation simulated in the ncep climate forecast system model: The importance of stratiform heating. *J. Climate*, **23 (18)**, 4770–4793.

Stan, C., D. M. Straus, J. S. Frederiksen, H. Lin, E. D. Maloney, and C. Schumacher, 2017: Review of tropical-extratropical teleconnections on intraseasonal time scales. *Rev. Geophys.*, **55 (4)**, 902–937.

Stechmann, S. N., and A. J. Majda, 2009: Gravity waves in shear and implications for organized convection. *J. Atmos. Sci.*, **66 (9)**, 2579–2599.

Tao, W.-K., and M. W. Moncrieff, 2009: Multiscale cloud system modeling. *Rev. Geophys.*, **47 (4)**.

Tung, W.-W., and M. Yanai, 2002a: Convective momentum transport observed during the TOGA COARE IOP. part I: General features. *J. Atmos. Sci.*, **59 (11)**, 1857–1871.

Tung, W.-W., and M. Yanai, 2002b: Convective momentum transport observed during the TOGA COARE IOP. part II: Case studies. *J. Atmos. Sci.*, **59 (17)**, 2535–2549.

Xing, Y., A. J. Majda, and W. W. Grabowski, 2009: New efficient sparse space–time algorithms for superparameterization on mesoscales. *Mon. Wea. Rev.*, **137 (12)**, 4307–4324.

Yanai, M., B. Chen, and W.-w. Tung, 2000: The Madden–Julian oscillation observed during the TOGA COARE IOP: Global view. *J. Atmos. Sci.*, **57 (15)**, 2374–2396.

Yang, Q., and A. J. Majda, 2014: A multi-scale model for the intraseasonal impact of the diurnal cycle of tropical convection. *Theor. Comput. Fluid Dyn.*, **28 (6)**, 605–633.

Yang, Q., and A. J. Majda, 2017: Upscale impact of mesoscale disturbances of tropical convection on synoptic-scale equatorial waves in two-dimensional flows. *J. Atmos. Sci.*, **74 (9)**, 3099–3120.

Yang, Q., and A. J. Majda, 2018a: Upscale impact of mesoscale disturbances of tropical convection on 2-day waves. *accepted by Journal of the Atmospheric Sciences*.

Yang, Q., and A. J. Majda, 2018b: Upscale impact of mesoscale disturbances of tropical convection on convectively coupled kelvin waves. *J. Atmos. Sci.*, **75 (1)**, 85–111.

Yang, Q., A. J. Majda, and B. Khouider, 2017: ITCZ breakdown and its upscale impact on the planetary-scale circulation over the eastern pacific. *J. Atmos. Sci.*, **74 (12)**, 4023–4045.

Zhang, C., 2005: Madden-Julian oscillation. *Rev. Geophys.*, **43 (2)**.

Zhang, C., 2013: Madden–Julian oscillation: Bridging weather and climate. *Bull. Amer. Meteor. Soc.*, **94 (12)**, 1849–1870.

Zhang, G. J., and N. A. McFarlane, 1995: Role of convective scale momentum transport in climate simulation. *Journal of Geophysical Research: Atmospheres*, **100 (D1)**, 1417–1426.

Zhang, G. J., and X. Song, 2009: Interaction of deep and shallow convection is key to Madden-Julian Oscillation simulation. *Geophys. Res. Lett.*, **36 (9)**.

LIST OF TABLES

TABLE 1. Prognostic governing equations in the 2D multicloud model for the MJO analog and intraseasonal variability above the equator.

Name	Equation
Momentum, jth-baroclinic mode, $j=1,2$	$\frac{\partial u_j}{\partial t} = \frac{\partial \theta_j}{\partial x} - \frac{C_d u_0}{h_b} u_j - \frac{1}{\tau_R} u_j + F_j^u$
Potential temperature, first-baroclinic mode	$\frac{\partial \theta_1}{\partial t} - \frac{\partial u_1}{\partial x} = P - Q_{R,1}^0 - \frac{1}{\tau_D}\theta_1 + F_1^\theta$
Potential temperature, second-baroclinic mode	$\frac{\partial \theta_2}{\partial t} - \frac{1}{4}\frac{\partial u_2}{\partial x} = -H_s + H_c - Q_{R,2}^0 - \frac{1}{\tau_D}\theta_2 + F_2^\theta$
Free tropospheric moisture	$\frac{\partial q}{\partial t} + \frac{\partial}{\partial x}\left[(u_1 + \tilde{\alpha} u_2) q + \tilde{Q}\left(u_1 + \tilde{\lambda} u_2\right)\right] = -\frac{2\sqrt{2}}{\pi} P + \frac{D}{H_T}$
Boundary-layer equivalent potential temperature	$\frac{\partial \theta_{eb}}{\partial t} = \frac{1}{h_b}(E - D)$
Congestus heating	$\frac{\partial H_c}{\partial t} = \frac{1}{\tau_c}\left(\alpha_c \frac{\Lambda - \Lambda^*}{1-\Lambda^*}\frac{D}{H_T} - H_c\right)$
Stratiform heating	$\frac{\partial H_s}{\partial t} = \frac{1}{\tau_s}(\alpha_s P - H_s)$

TABLE 2. Diagnostic equations in the 2D multicloud model for the MJO analog and intraseasonal variability above the equator. The notation bar indicates the value of variables at RCE state. The notation f^+ represents positive value of f and vanishes when $f < 0$, that is, $f^+ = max\{f, 0\}$.

Name	Equation
Mid-tropospheric equivalent potential temperature	$\theta_{em} = q + \frac{2\sqrt{2}}{\pi}\left(\theta_1 + \alpha_2\theta_2\right)$
Switch function for mid-tropospheric dryness	$\Lambda = \begin{cases} 1 & if\ \bar{\theta}_{eb} - \bar{\theta}_{em} + \theta_{eb} - \theta_{em} \geq 20\,K \\ linear & between \\ \Lambda^* & if\ \bar{\theta}_{eb} - \bar{\theta}_{em} + \theta_{eb} - \theta_{em} \leq 10\,K \end{cases}$
Deep heating	$P = \frac{1-\Lambda}{1-\Lambda^*}P_0$ $= \frac{1-\Lambda}{1-\Lambda^*}\left[\bar{Q} + \frac{1}{\tau_{conv}}\left(a_1\theta_{eb} + a_2 q - a_0\left(\theta_1 + \gamma_2\theta_2\right)\right)\right]^+$
Downdrafts	$D = \Lambda D_0$ $= \Lambda m_0\left[1 + \mu_2\frac{H_s - H_c}{\bar{P}}\right]^+\left(\bar{\theta}_{eb} - \bar{\theta}_{em} + \theta_{eb} - \theta_{em}\right)$
Surface evaporation flux	$\frac{E}{h_b} = \frac{1}{\tau_e}\left(\theta^*_{eb} - \bar{\theta}_{eb} - \theta_{eb}\right)$

TABLE 3. Parameters and constants in the idealized GCM with clear deficiencies. The different value of parameters and constants used for the realistic MJO analog above the equator is shown in the bracket. All the remaining ones are the same as Majda et al. (2007).

Name	Symbol	Value
First baroclinic radiative cooling rate	$Q_{R,1}^0$	$1\ K/day$
Stratiform adjustment coefficient	α_s	0.125 (0.25)
Congestus adjustment coefficient	α_c	0.25 (0.5)
Height of troposphere	H_T	15.7 km
Height of the boundary layer	h_b	500 m
Relative contribution of stratiform and congestus to downdrafts	μ_2	0.5
Convective time scale	τ_{conv}	12 hrs
Momentum drag time scale due to turbulent fluctuations	τ_{tur}	28.9 days
Rayleigh-wind relaxation time scale	τ_R	150 days
Newtonian cooling time scale	τ_D	100 days
Stratiform adjustment time scale	τ_s	7 days
Congestus adjustment time scale	τ_c	7 days
Inverse convective buoyancy time scale of deep clouds	a_0	12
Relative contribution fraction of θ_{eb} to deep convection	a_1	0.1
Relative contribution fraction of q to deep convection	a_2	0.9
Relative contribution of θ_2 to deep heating	γ_2	0.1
Relative contribution of θ_2 to θ_{em}	α_2	0.1
Coefficient of $\mathbf{v_2}$ in nonlinear moisture convergence	$\tilde{\alpha}$	0.1
Coefficient of $\mathbf{v_2}$ in linear moisture convergence	$\tilde{\lambda}$	0.6
Background moisture stratification	$\tilde{Q}$	1.03 (1.0)
Lower threshold of the switch function Λ	Λ^*	0.2

TABLE 4. Value of thermodynamic variables at RCE state. The remaining variables not mentioned here are all zero. The different values of parameters and constants used for the realistic MJO analog above the equator is shown in the brackets.

Name	Symbol	Value
Discrepancy between boundary layer and middle troposphere θ_e	$\bar{\theta}_{eb} - \bar{\theta}_{em}$	12 K
Discrepancy between boundary layer θ_e and its saturated value	$\theta^*_{eb} - \bar{\theta}_{eb}$	10 K
Moisture switch at RCE	$\bar{\Lambda}$	0.36
Bulk convective heating at RCE	$\bar{Q}$	1.25 $Kday^{-1}$
Congestus heating at RCE	$\bar{H}_c$	0.045 $Kday^{-1}$ (0.09 $Kday^{-1}$)
Deep heating at RCE	$\bar{H}_d$	1 $Kday^{-1}$
Stratiform heating at RCE	$\bar{H}_s$	0.125 $Kday^{-1}$ (0.25 $Kday^{-1}$)
Second baroclinic radiative cooling rate	$Q^0_{R,2}$	-0.08 $Kday^{-1}$ (-0.16 $Kday^{-1}$)
Downdraft mass flux reference scale	m_0	0.0364 ms^{-1} (0.035 ms^{-1})
Evaporation time scale	τ_e	8.49 hrs

TABLE 5. Summary of all experiments under the different model setup and their results in capturing key features of the MJO. In the “upscale impact of MCSs” column, “no” means no eddy is added, “westward/eastward” means the propagation direction of MCSs, “slow/fast” corresponds to 5/20 ms^{-1}, “upshear/downshear” means the propagation direction of MCSs is opposite/along vertical shear direction. The “modulation” column shows the modulation effects of deep heating excess P_0 and vertical shear strength. The “key feature” column includes (1) two-scale structure of the MJO analog, (2) wavenumber-frequency spectra of precipitation and winds with planetary/intraseasonal peaks, (3) westerly wind burst.

Experiments	Model Setup		Key Feature			Figure
	upscale impact of MCSs	modulation	two-scale	spectra	WWB	
Realistic MJO analog	no	N/A	**good**	**good**	**good**	Fig.1
Idealized GCM with clear deficiencies	no	N/A	bad	bad	bad	Fig.2
Improved simulations by the parameterization of upscale impact of MCSs	westward, slow	P_0	**good**	**good**	bad	Fig.4b,5c,5d,6a
	westward, fast	P_0	bad	**good**	bad	Fig.4c,5e,5f,6b
	westward, slow	shear	**good**	bad	bad	Fig.8b,9c,9d,10a
	upshear, slow	shear	bad	bad	**good**	Fig.8c,9e,9f,10b
	downshear, slow	shear	bad	not shown	not shown	Fig.8d
	upshear, slow	P_0 & shear	**good**	**good**	**good**	Fig.11,12,13

LIST OF FIGURES

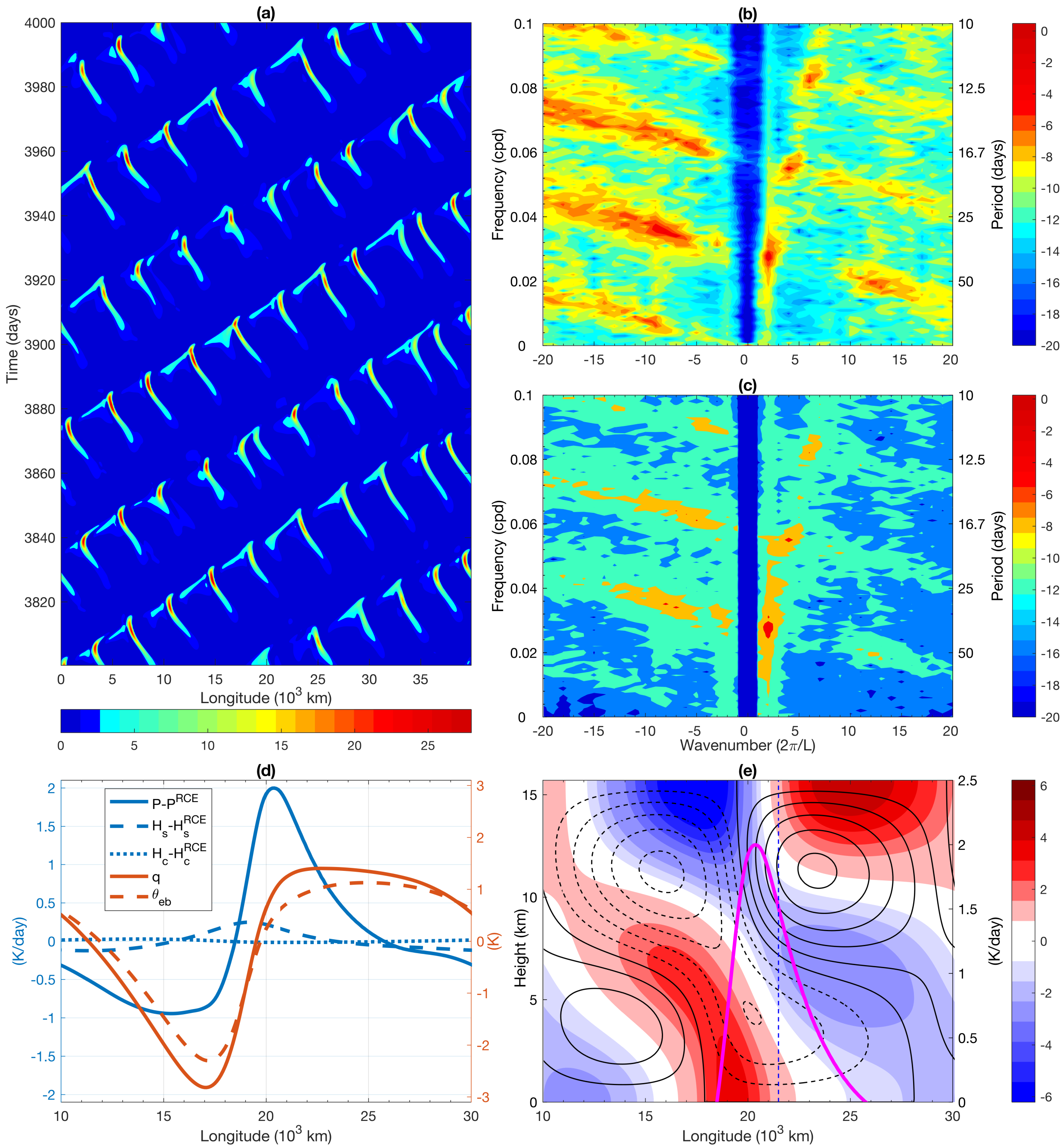

FIG. 1. Realistic MJO analog above the equator. Hovmöller diagram for (a) precipitation ($\frac{2\sqrt{2}}{\pi}P$) and log-scale wavenumber-frequency spectra for (b) precipitation and (c) surface-level zonal velocity ($\sqrt{2}u_1+\sqrt{2}u_2$), (d-e) vertical cross-sections of composite planetary-scale envelope in the moving reference frames (6.1 ms^{-1}), based on model output between day 3000 and day 4000. Panels (d) shows deep heating (P), stratiform heating (H_s) and congestus heating (H_c) with the left y-axis and moisture (q), boundary-layer equivalent potential temperature (θ_{eb}) with the right y-axis. Panel (e) shows zonal velocity (u, color) and potential temperature (θ, solid lines for positive value, dashed lines for negative, contour interval 0.05K). The pink curve shows the zonal profile of precipitation anomalies with the right axis. The vertical dashed line indicates the longitude with easterly (west-

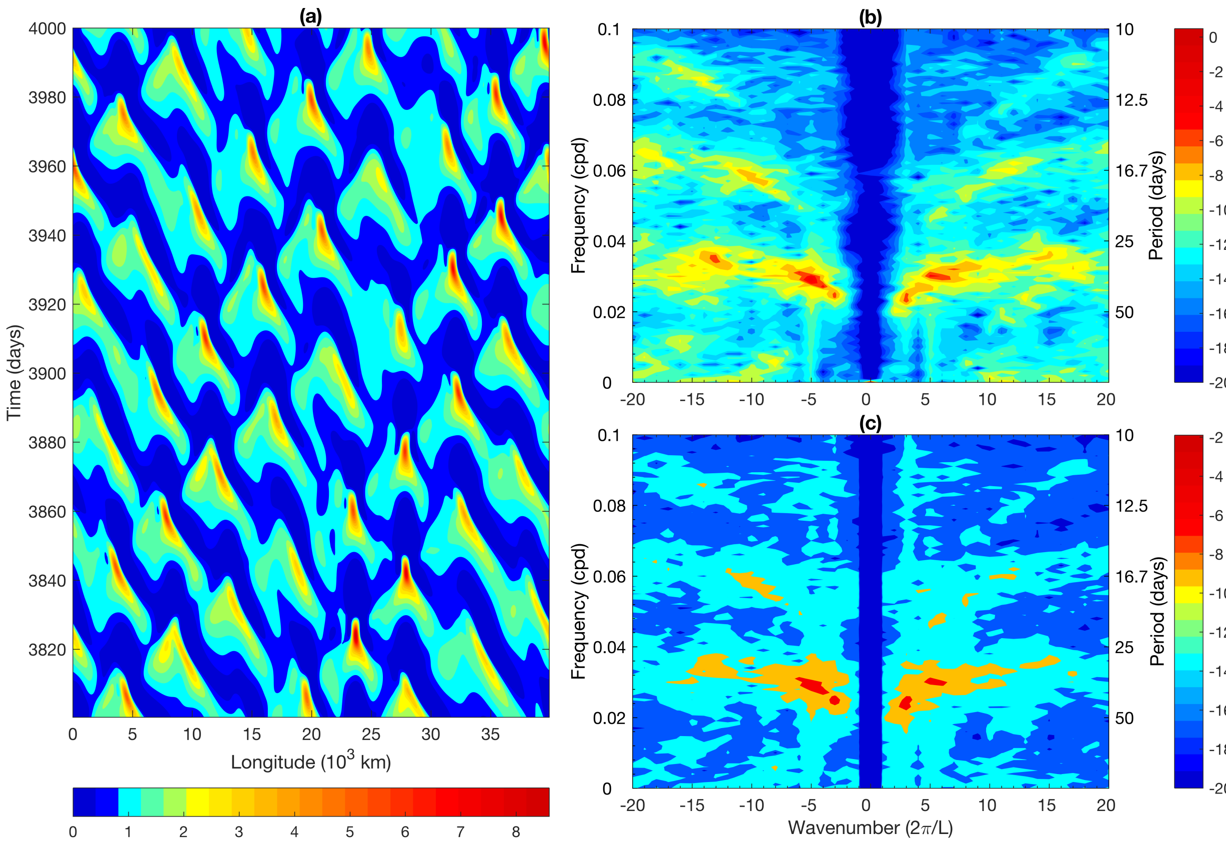

FIG. 2. An idealized GCM with clear deficiencies. Hovmöller diagram for (a) precipitation ($\frac{2\sqrt{2}}{\pi}P$) and log-scale wavenumber-frequency spectra for (b) precipitation and (c) surface-level zonal velocity ($\sqrt{2}u_1 + \sqrt{2}u_2$) based on model output between day 3000 and day 4000. The units of precipitation and zonal velocity are $Kday^{-1}$, ms^{-1}, respectively.

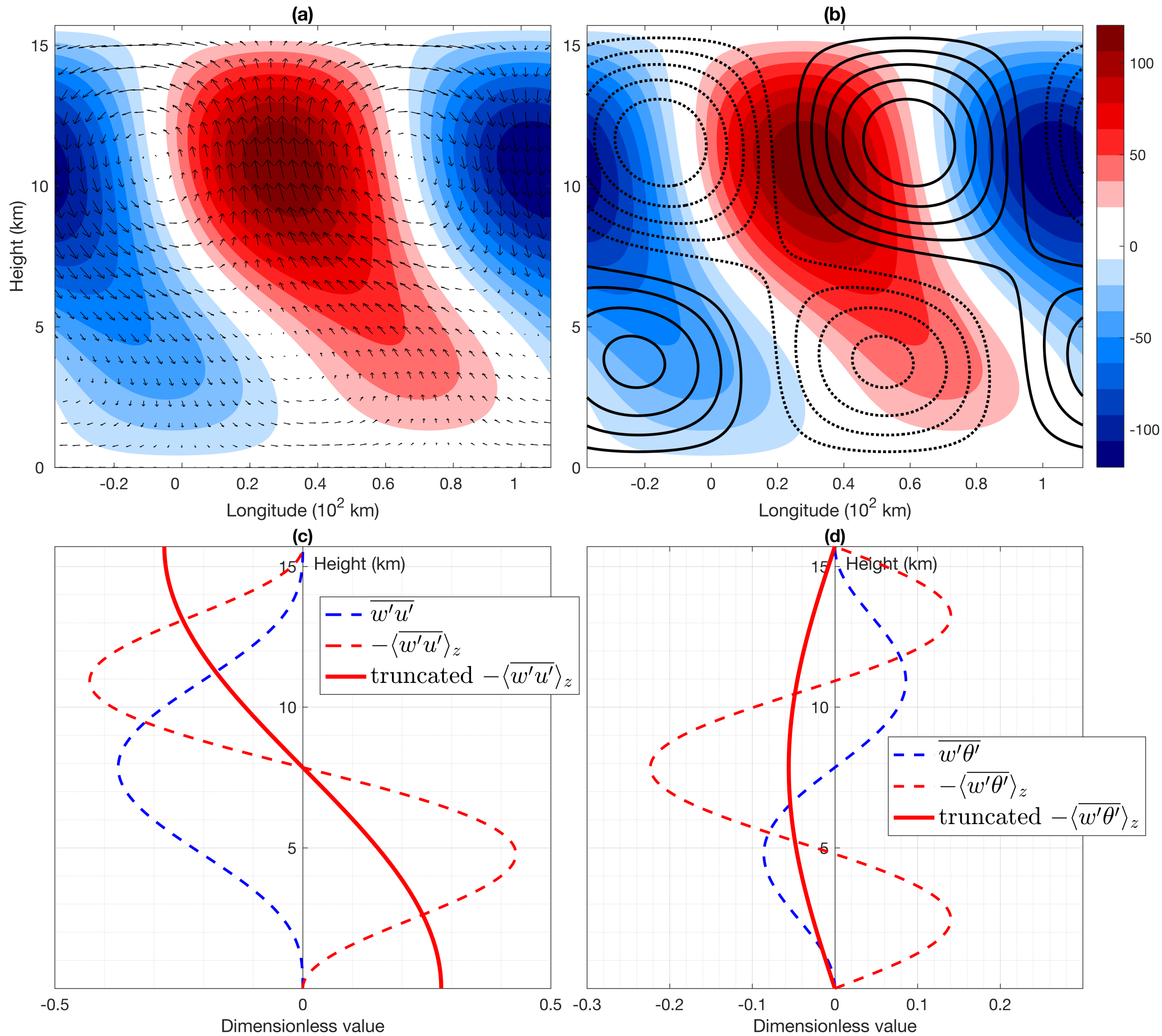

989 FIG. 3. Vertical profiles of (a) zonal/vertical velocity (u', w', arrows), (b) potential temperature anomalies (θ', contours interval 0.06 K), (c) eddy momentum transfer ($-\left\langle\overline{w'u'}\right\rangle_z$) and (d) eddy heat transfer ($-\left\langle\overline{w'\theta'}\right\rangle_z$) in an eastward-moving mesoscale system. The colors in panels (a,b) show mesoscale heating (s'_θ). The maximum magnitudes of zonal and vertical velocities are $3.73ms^{-1}$ and $0.47ms^{-1}$, respectively. Panels (c,d) also show truncated eddy transfer of momentum and temperature with only the first-baroclinic mode. One dimensionless unit of eddy momentum transfer and eddy heat transfer is 15 $ms^{-1}day^{-1}$ and 4.5 $Kday^{-1}$, respectively.

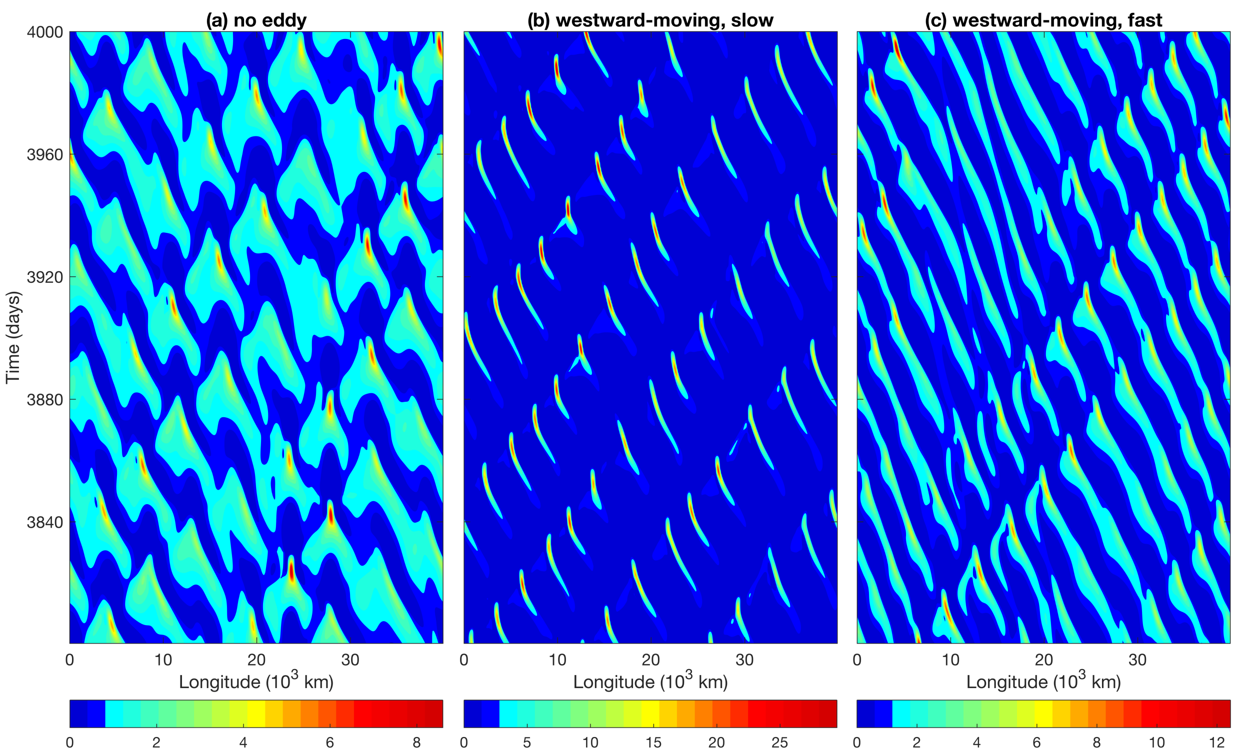

FIG. 4. Hovmöller diagrams for precipitation ($\frac{2\sqrt{2}}{\pi}P$) between day 3800 and day 4000 in the cases with/without eddy terms from westward-moving MCSs modulated by the deep heating excess (P_0). Panel (a) shows the case without eddy terms. Panels (b-c) show the case with eddy terms from (b) slowly propagating MCSs ($5\ ms^{-1}$) and (c) fast propagating MCSs ($20\ ms^{-1}$). The unit is $Kday^{-1}$.

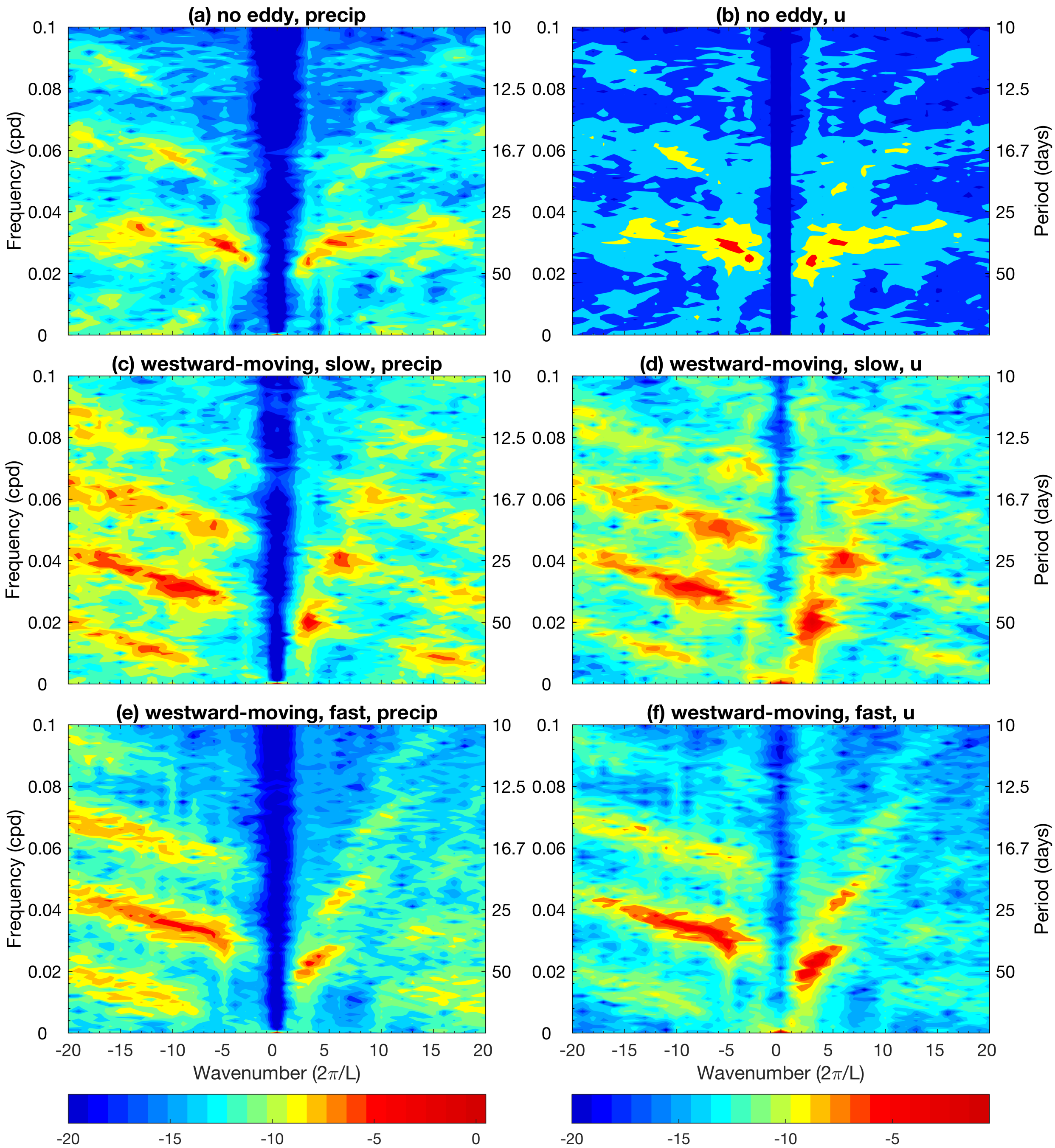

FIG. 5. Log-scale wavenumber-frequency spectra of precipitation ($\frac{2\sqrt{2}}{\pi}P$, left column) and surface-level zonal velocity ($\sqrt{2}u_1 + \sqrt{2}u_2$, right column) in the wavenumber-frequency diagrams, based on the model output between day 3000 and day 4000 in the cases with/without eddy terms from westward-moving MCSs modulated by the deep heating excess (P_0). The rows from top to bottom correspond to the case with (a,b) no eddy, (c,d) eddy terms from slowly propagating MCSs (5 ms^{-1}), (e,f) eddy terms from fast propagating MCSs (20 ms^{-1}). Each column share the same color as placed in the bottom.

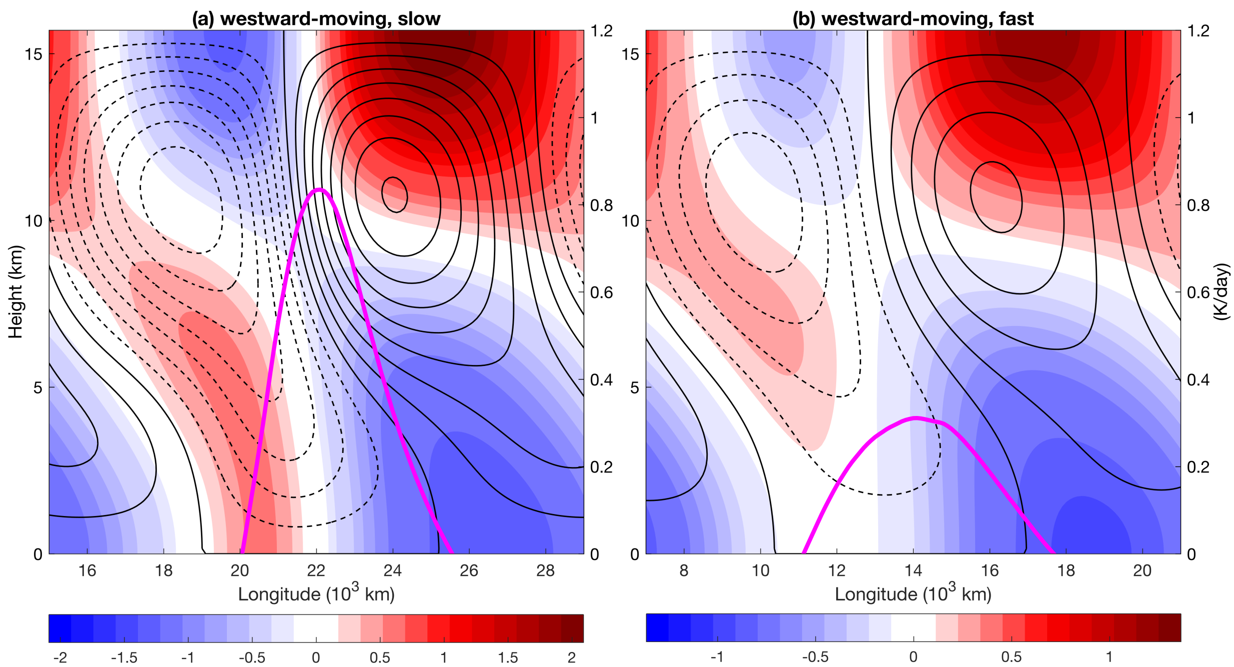

FIG. 6. Vertical cross-sections of composite planetary-scale envelope in the moving reference frames (s is the propagation speed), based on model output between day 3000 and day 4000 in the cases with eddy terms from westward-moving MCSs modulated by the deep heating excess (P_0). Panels (a-b) show the cases with eddy terms from (a) slowly propagating MCSs (5 ms^{-1}) and s=3.05 ms^{-1}, and (b) fast propagating MCSs (20 ms^{-1}) and s=3.35 ms^{-1}. Zonal velocity (u) is shown by color and potential temperature (θ) is shown by contours (solid lines for positive value, dashed lines for negative, contour interval 0.005K). The pink curve shows the zonal profile of precipitation anomalies ($\frac{2\sqrt{2}}{\pi}P$) with the right axis. Domain-mean potential temperature is removed. The units of zonal velocity and potential temperature are ms^{-1},K, respectively.

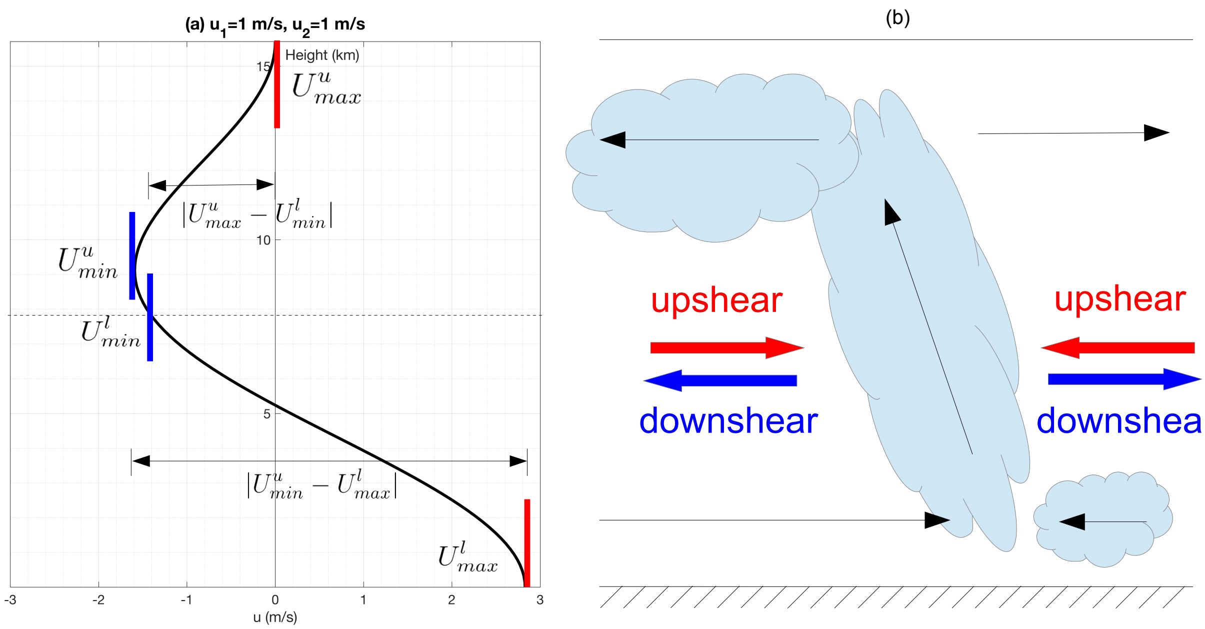

FIG. 7. A conceptual diagram for the definition of (a) vertical shear strength ($|\triangle U|$) and (b) upshear/downshear propagation. In panel (a), the red (blue) bars indicate the maximum (minimum) magnitude of zonal winds in the upper and lower tropospheres. The strength of vertical shear is defined as the stronger magnitude between westerly and easterly vertical shear, $|\triangle U| = max\left\{\left|U^u_{max} - U^l_{min}\right|, \left|U^u_{min} - U^l_{max}\right|\right\}$, and its direction ($sign(\triangle U)$) is determined correspondingly. Panel (b) describes an eastward-moving MJO analog with wind convergence (divergence) in the lower (upper) troposphere. According to the deifinition of vertical shear in panel (a), this MJO analog is accompanied by easterly (westerly) vertical shear to the west (east). Upshear (downshear) is defined as propagation along the opposite (same) direction of vertical shear.

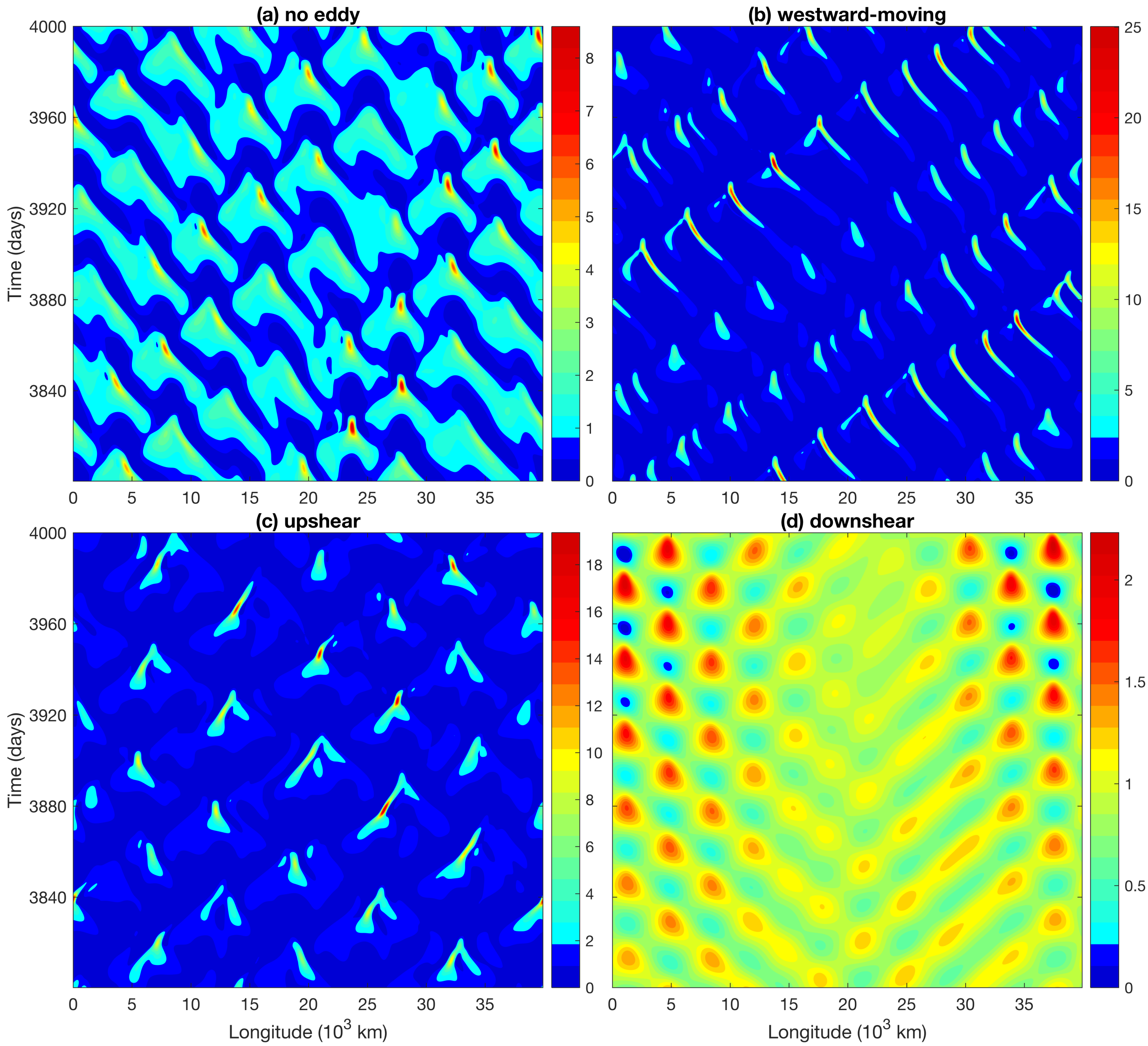

1021 FIG. 8. Similar to Fig.4 but the cases with/without eddy terms modulated by vertical shear strength ($|\triangle U|$).
1022 Panel (a) shows the case without eddy terms. The remaining panels shows the case with eddy terms from MCSs
1023 propagating at a slow speed and (b) westward, (c) upshear, (d) downshear.

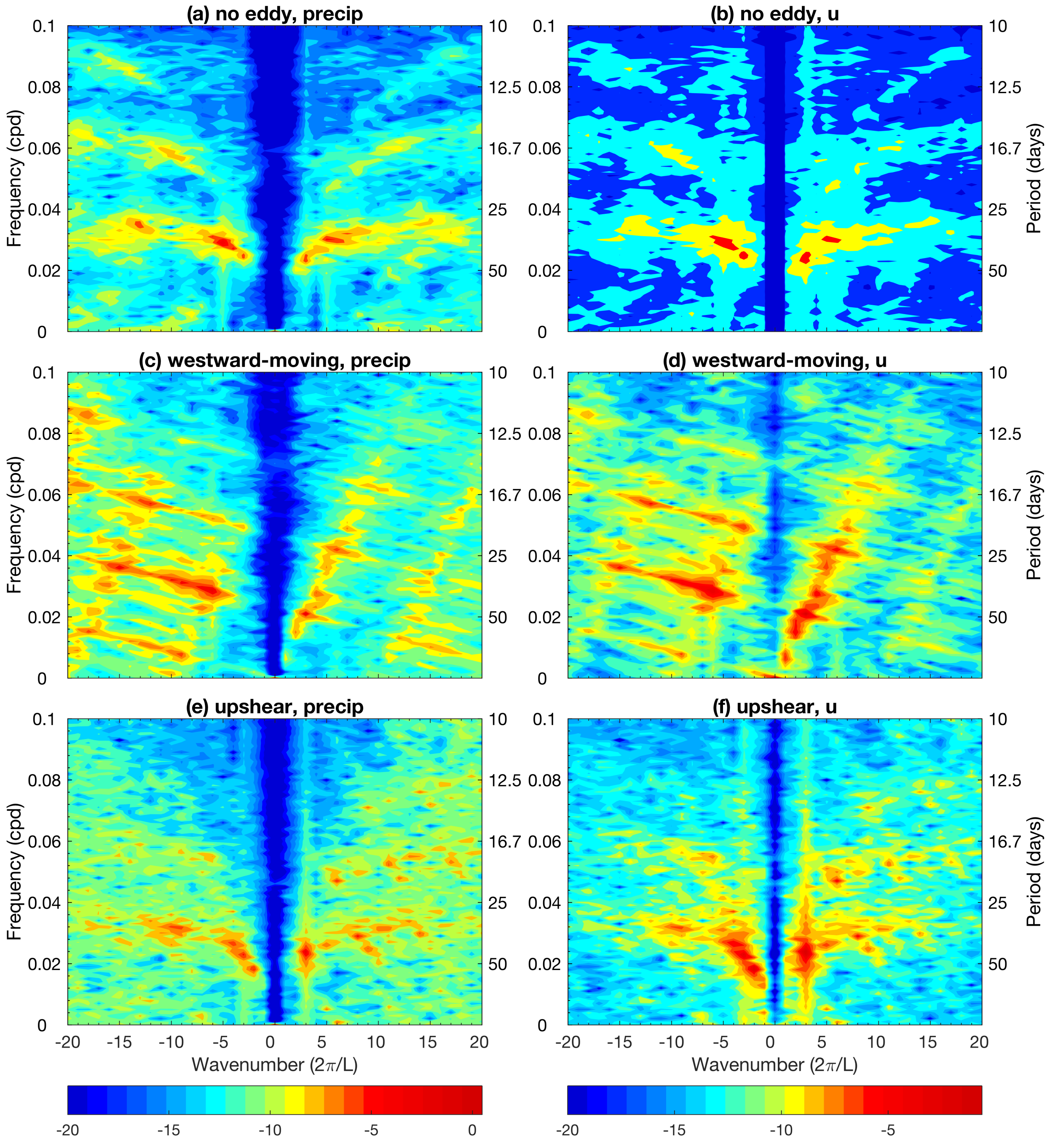

1024 FIG. 9. Similar to Fig.5 but for the cases with/without eddy terms modulated by the vertical shear strength
1025 ($|\triangle U|$). The rows from top to bottom correspond to the case with (a,b) no eddy, (c,d) eddy terms from westward-
1026 moving MCSs, (e,f) eddy terms from upshear-moving MCSs.

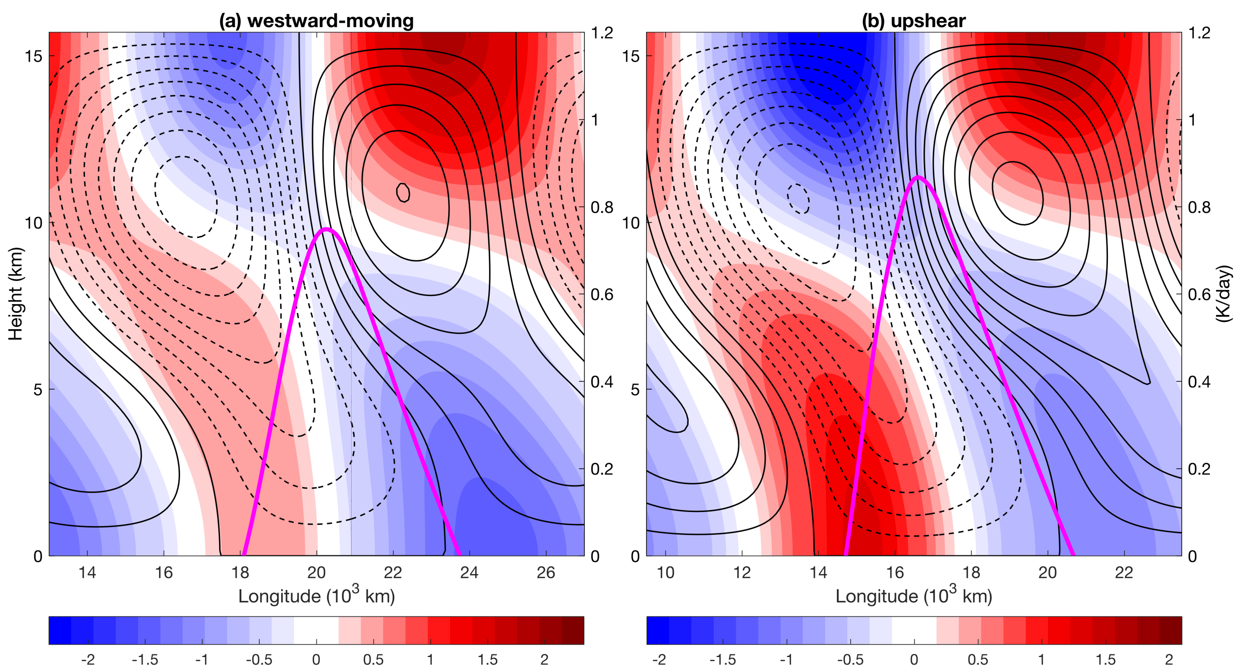

1027 FIG. 10. Similar to Fig.6 but the cases with eddy terms modulated by the vertical shear strength ($|\triangle U|$). Panel
1028 (a-b) show the cases with eddy terms from (a) westward-moving MCSs and s=3.075 ms^{-1}, and (b) upshear-
1029 moving MCSs and s=3.5 ms^{-1}.

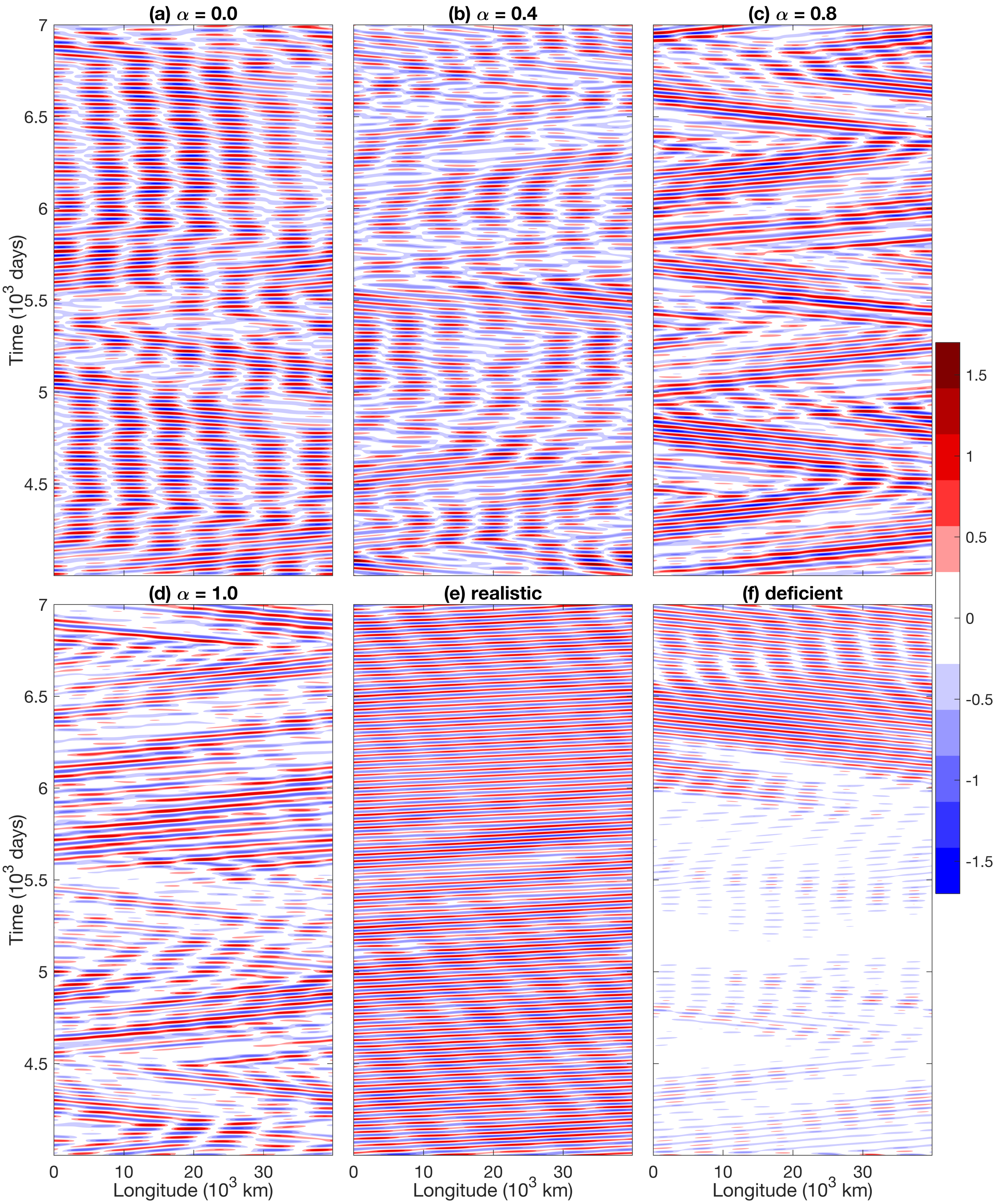

FIG. 11. Hovmöller diagrams for planetary/intraseasonal anomalies (deviation from RCE value) of precipitation ($\frac{2\sqrt{2}}{\pi}P$) between day 4000 and day 7000. Panels (a-d) correspond to the cases with α equal to (a) 0.0, (b) 0.4, (c) 0.8, (d) 1.0. Panels (e) and (f) correspond to the cases in Fig.1a and Fig.2a, respectively. The planetary/intraseasonal anomalies are obtained by using a low-pass filter and only those on length scale larger than 10000 km and time scale longer than 30 days are retained. The unit is $Kday^{-1}$.

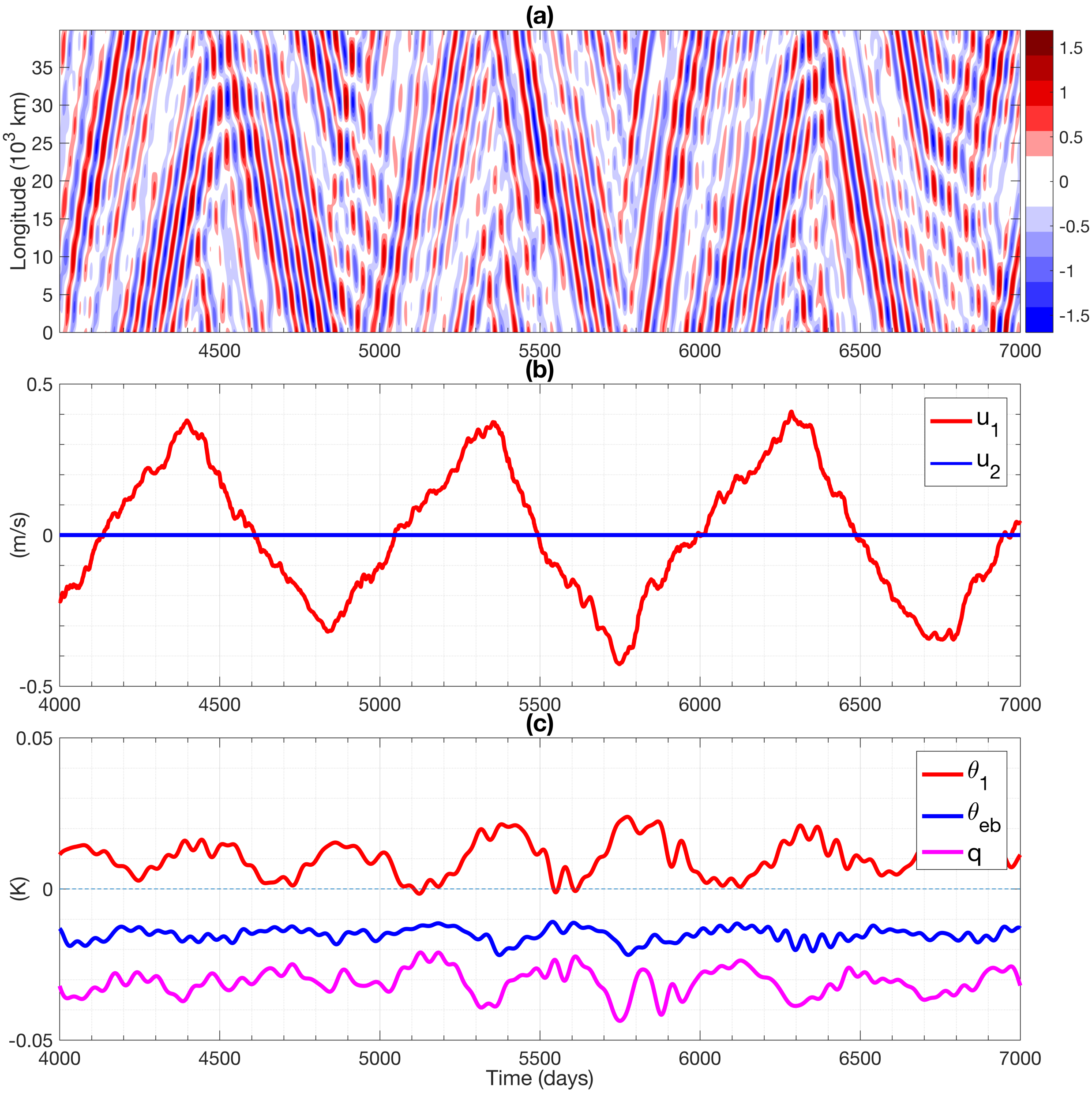

FIG. 12. Time series of precipitation, zonal velocity and thermodynamical fields between day 4000 and day 7000. Panel (a) shows the Hovmöller diagram for planetary/intraseasonal anomalies of precipitation (the same as Fig.11c), while panel (b) and (c) show domain-mean zonal velocity (u_1 and u_2) and thermodynamic fields (first-baroclinic potential temperature θ_1, boundary-layer equivalent potential temperature θ_{eb}, moisture q) during the same period, respectively. Only anomalies of these thermodynamic fields (θ_1,θ_{eb},q) on the time scale longer than 50 days are retained by using the low-pass filter. The units of precipitation and zonal velocity are $Kday^{-1}$, ms^{-1}, respectively.

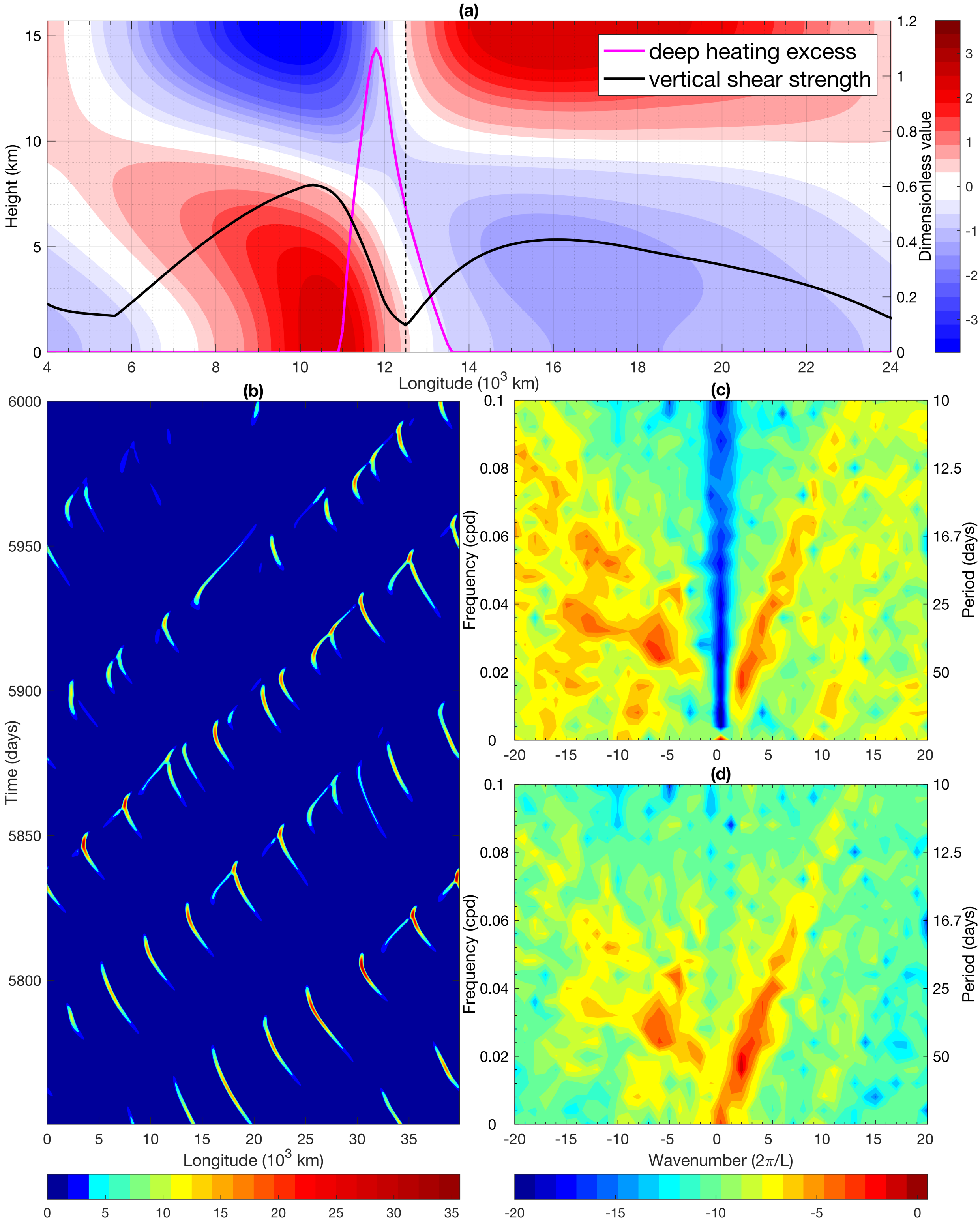

FIG. 13. An idealized GCM with clear deficiencies and extra parameterization for upscale impact of MCSs with $\alpha = 0.8$. Panel (a) shows vertical cross-sections of composite planetary-scale envelope in the moving reference frames (3.65 ms^{-1}) based on model output between day 5750 and day 6000. Zonal velocity (u) is shown by color. Dimensionless value of deep heating excess ($\frac{P_0}{\bar{Q}}$) is shown by pink curve, while that of vertical

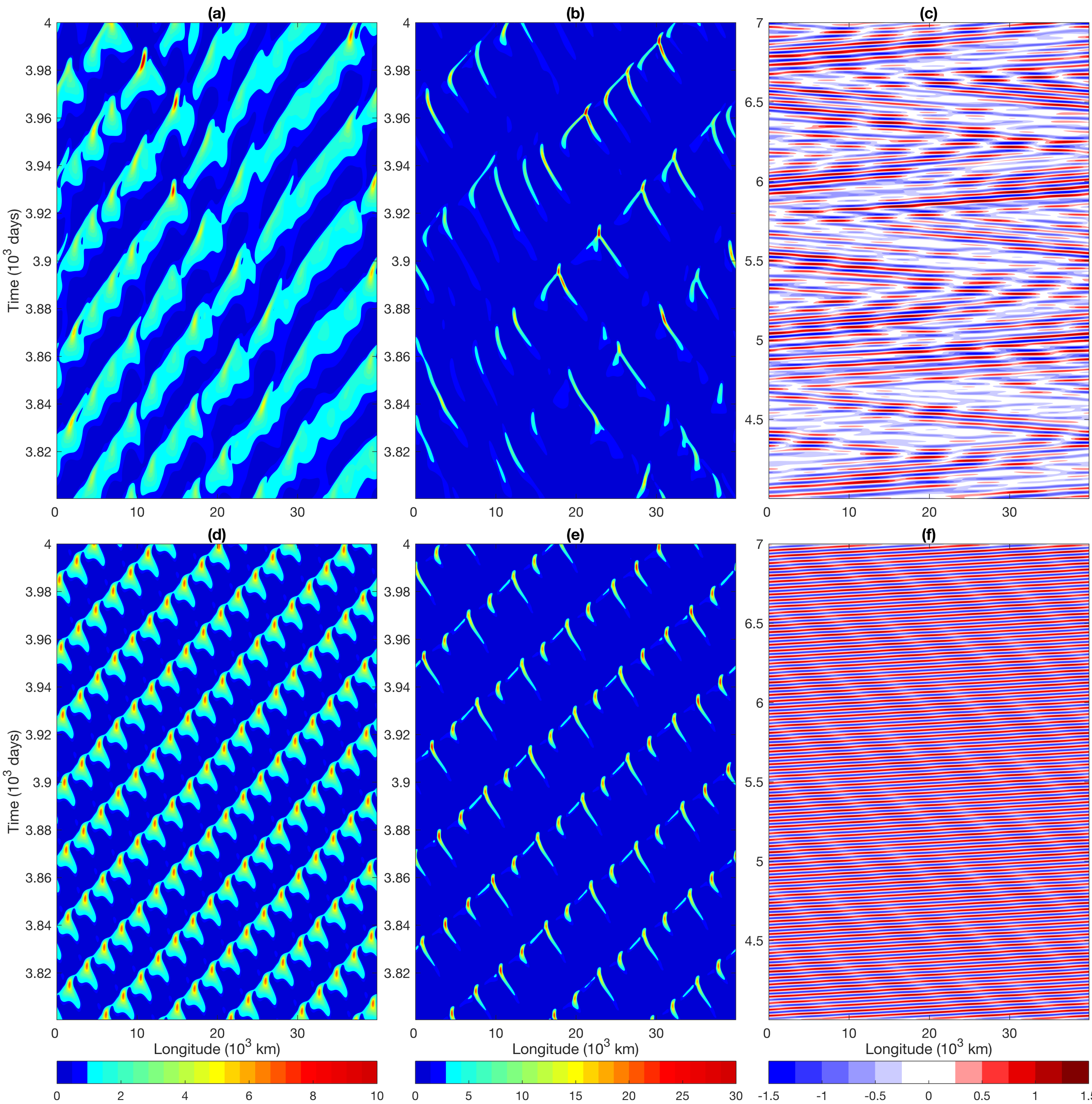

1051 FIG. 14. Hovmöller diagrams for precipitation from deficient GCMs and improved simulations by the parameterization of upscale impact of MCSs. Panel (a) shows the solutions from the deficient GCM with $\tilde{Q} = 1.03$ and $\tilde{\lambda} = 0.3$ between day 3800 and day 4000. Panel (b) shows the improved simulation by the parameterization during the same period. Panel (c) shows planetary/intraseasonal anomalies from the improved simulation between day 4000 and day 7000 by using the same low-pass filter as Fig.11. Panels (d-f) are similar to panels (a-c) but for the other deficient GCM with $a_0 = 32$. Panels in each column share the same colorbar in the bottom. The unit of precipitation is $Kday^{-1}$.